Chapter 3

Ice Loss Experiments

3.1 Chapter Summary

This chapter describes a set of experiments to measure diffusion coefficients, D, in unconsolidated porous materials at Mars-like conditions. The materials chosen are simple proxies for real Mars soils, of which no samples or small-scale data currently exist. The experiments were designed to closely reproduce the conditions under which sublimative ice loss to a relatively dry atmosphere occurs on Mars. Thus, solid ice acted as the source for the diffusing species, gaseous H_2O. The diffusion host gas was CO_2 at ∼600 Pa pressure and the whole environment was maintained below the freezing point of water.

Four materials were used to simulate the martian regolith with varying degrees of fidelity or with a particular focus. Despite the differences between these simulants, the range of diffusion coefficients measured (including micron-sized dust) fell between approximately 2.8–5.4 $cm^2\ s^{-1}$, though for mechanically packed dust lower values of $0.38 \pm 0.26\ cm^2\ s^{-1}$ were observed.

The survival of shallow subsurface ice on Mars and the providence of diffusion barriers are considered in light of these measurements.

3.2 Experimental

The experiments were conducted at the Mars Simulation and Ice Laboratory at Caltech. Custom built stainless-steel vacuum chambers contained within walk-in freezers were used to achieve Mars-like conditions of temperature, pressure, and low humidity.

These experiments simulate the evolution of near-surface ice on present-day Mars inasmuch as the atmosphere is very dry with a frost point well below the temperature of the ice. Thus the ice is driven to sublimate into the atmosphere resulting in a loss of mass of the regolith-ice-container system. Although the conditions may not replicate any particular location on Mars (being too warm, in general, for regions expected to possess subsurface ice today) they do emulate the geometry and

fundamentally important physics for the investigation of vapor diffusion.

The source of water vapor in these diffusion experiments is a block of ice made from purified water. The ice is frozen in the presence of both a heat source to retard surface freezing and a bubbler to provide mechanical agitation. This procedure allows most gases exsolved upon freezing to escape through the top surface, resulting in a cylinder of largely bubble-free ice.

Ice samples are cut from the cylinder in 1-cm-thick slices and frozen with a small amount of additional water into plastic caddies ∼7 cm in diameter. The caddy heights, being 2, 3, 6, and 11 cm, permit sample thicknesses over the ice of 1, 2, 5, and 10 cm, respectively. See Figure 3.2 a) for an example of a 2 cm caddy with ice and thermocouple in place.

3.2.1 Chamber setup

A custom built stainless-steel vacuum chamber from LACO Technologies was used to perform these ice-loss experiments. In basic design the chamber is a vertical cylinder with a removable lid, silicone O-ring seals, and multiple electrical and fluid feedthroughs. A schematic of the chamber with sample and measurement apparatus is shown in Figure 3.1. The volume of the chamber is 2.3×10^{-2} m^3.

During an experiment, an Alcatel rotary vacuum pump continuously evacuates the chamber at an effective pumping speed of 0.34 m^3 hr^{-1}. The pressure is monitored with a Baratron capacitance manometer with a full-scale range of 10 torr. Evacuation is compensated by input of dry CO_2 regulated with an MKS PDR 2000 gauge controller connected to either 1) a normally-open solenoid valve (earlier experiments) or 2) an active PID closed-loop control using an STEC-4400 mass flow controller (MFC). The setpoint of the MFC is controlled via an output channel on a USB-1408FS datalogger from Measurement Computing Corporation. The PID algorithm and datalogger are run through the LabView development environment. The total pressure is maintained at ∼600 Pa in the case of the solenoid valve control, and at a more uniform 586 ± 0.1 Pa in the case of the MFC. The continuous replacement of chamber gas in either case results in a very dry atmosphere above the samples (see Figure 3.2 b).

Decompression of the dry CO_2 from its holding cylinder and passage through gas loops in the freezers produces a stable chamber air temperature approximately equal to the ambient freezer temperature. The walk-in freezers are on a 12-hour defrost cycle which results in twice-daily temperature spikes of approximately 0.5 K. These perturbations to the environment decayed in about 60 minutes prior to a compressor upgrade in April of 2007. Following the upgrade, the perturbations were much smaller and lasted less than 30 minutes. Fiberglass and Styrofoam insulation around the chamber minimizes these fluctuations.

Water content in the chamber atmosphere is monitored using capacitive relative humidity (RH) chips from Honeywell (HIH-3602-C). These integrated-circuit sensors contain both an RH proportional voltage output and a 1000 ohm platinum resistance temperature device (RTD) which is

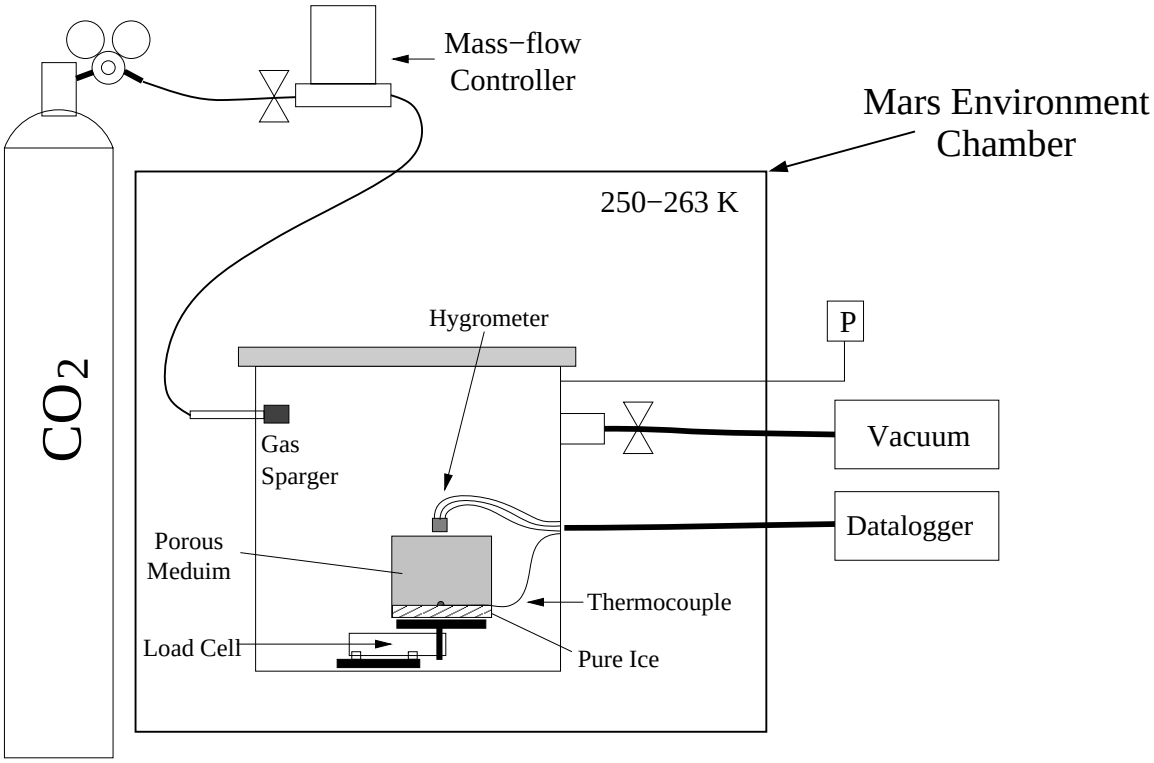

Figure 3.1: Schematic of the diffusive ice-loss experimental setup. The main environmental chamber is housed within a walk-in freezer with temperatures of 250–263 K. The CO_2 atmosphere is constantly exchanged and maintained at 600 Pa total pressure. Gas entering the chamber is passed through a diffusing sparger to minimize directed air currents. Temperature, humidity, mass, and pressure data are recorded by a datalogger which resides outside the cold room.

measured in a 3-wire half-bridge configuration. The RH chips are reported by the manufacturer to be accurate down to temperatures of 233 K and 0% relative humidity. The combined RH and temperature measurements allow the partial pressure of water at the sensors to be calculated. The sensors are positioned at the center of the sample tops within 1 cm of the surface (see Figure 3.2 c).

Sample mass is continuously monitored with Omega Engineering LCEB-5 strain gauge load cells (maximum capacity 5 lbs) in a wheatstone bridge configuration with an excitation of 5 V and an output of 2.0 mV/V. This instrument has a noise level of 0.2% of reading and a 0.03% full scale linearity. Mass-loss rates are calculated by monitoring the sample mass and drawing a linear regression through the values obtained over many hours.

The data from an experiment are recorded with a Campbell Scientific CR1000 data logger and saved to computer via the LoggerNet software package. The system is able to run two simultaneous experiments in a single vacuum chamber with identical ambient conditions by using dual load cells, thermocouples, and RH/RTD chips.

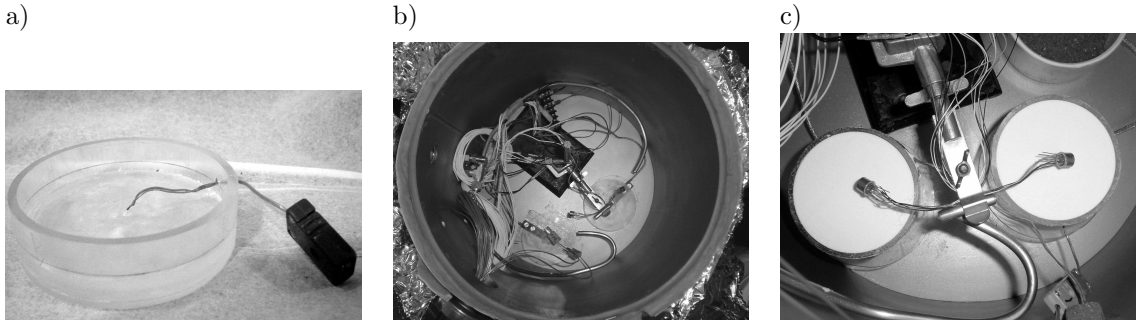

Figure 3.2: a) Closeup of thermocouple positioning in a caddy designed to accommodate 1 cm of ice and a 1 cm sample. The caddies are ∼7 cm in diameter. b) Down-looking view into the vacuum chamber (30 cm diameter) showing two load cells, gas and electrical feedthroughs, and RH/RTD chips attached to a ring-stand for positioning. c) A closeup of two glass bead samples in place with RH/RTD chips positioned 1 cm above sample surfaces

3.2.2 Experimental method

The mass of the ice-free caddy plus its thermocouple wire and connector is measured with a precision balance. After the 1 cm bubble-free ice disks are frozen into place, the combined system is weighed again. The total mass of ice and thereby its volume and thickness in the caddy can be determined. The media are poured into the caddies from their holding containers and planed off with a straight edge to match the height of the caddy. Most samples are not actively compressed, but may be subject to self-compaction. In most cases where self-compaction occurs, the sample surfaces remain within 1 mm of the caddy top. Some samples with very high dust fractions exhibit some settling as the container is moved from the preparation station to the vacuum chamber. This is at most 12% of the 5 cm sample depth. The reduced thickness is measured and included in subsequent calculations; additional material is not added.

The total mass of the entire sample assembly is measured, giving the total mass of simulant. The sample assembly is connected to the thermocouple feedthrough, placed on the load cell within the chamber, and the RH/RTD sensor is positioned above the sample. The chamber is sealed and pumped down to 600 Pa at a rate of ∼100 Pa per second. This slow pump-down prevents disturbance of the sample as any interstitial gases escape.

All steps described above are performed in a walk-in freezer at 263 K. The relative humidity of the freezer interior is quite high, usually around 80%, but the absolute humidity is low. Surface-melting, capillarity, and their effects on the initially dry simulant are thus minimized. Exposure of the samples to freezer air for the brief period between the storage vessel and the start of an experiment does not allow significant amounts of water to adsorb or freeze onto the simulant (as confirmed by water content measurements). Any minor amounts of water which adsorbs onto the sample is rapidly removed once introduced to the sublimation environment of the experiments.

Once the samples are in place and the chamber has reached Mars pressures, the experiment is

left to run for at least 12 hours. Transients due to adsorption of water in the sample or temperature disequilibrium decay after approximately two hours. The faster the mass-loss rate from the sample, the less time needed to obtain a sufficient number of points to ensure linearity and draw a regression line. For samples with a high impedance to gas flow, or for experiments run at lower temperatures, up to three days may be needed to achieve a high degree of confidence in the measurements.

Following the completion of an experimental run, the chamber is slowly purged to room-pressure; the slow back-fill prevents air currents from disturbing the sample. The sample material is dumped into a metal or glass vessel which is immediately weighed, then placed into an oven at 383 K. After 24 to 48 hours the sample is completely dry with respect to non-structural water and is weighed again. The sample is now dry and may be recycled for future experiments. Clumping of some materials containing smaller particles occasionally requires mechanical sieving to break up the aggregates.

Consolidated media such as glass fritted disks (described below) are epoxied in place inside glass rings with the same diameter as the ice caddies. During an experiment, these are placed over a 1 cm deep ice-filled caddy and secured in place with water-resistant vacuum grease. Following an experiment, the ice surface is examined to determine if any leaks occurred between the ice caddies and the glass rings. The low-pressure, low-temperature environment gives rise to distinct ice surface morphologies if the vapor escapes in a rapid or asymmetric way. Any experiments showing such leaks are discarded.

3.2.3 Measured quantities

All data for calculating diffusion coefficients is taken from the stable interval following initial transients. Additional small perturbations in temperature due to defrost cycling of the freezer compressor have no apparent effect on the mass loss curve and have a very small contribution to the average temperature value calculated for a 12+ hour experiment.

The mass loss rate is derived from a least-squares fit to the post-transient mass data versus time (see Figure 3.3). The temperature of the load cell fluctuates less than 1 K; there is no sensible temperature effect on the values reported. Residuals to the linear fit of mass loss are less than 1% in all experiments. Given the area of the sample surface (39.8 cm^2) and the density of ice, retreat rates in mm hr^{-1} and total H_2O flux are calculated.

A T-type thermocouple wire passes through the wall of each caddy 1 cm from the bottom and extends to the center of the cylinder. This wire is positioned on the surface of the ice disk and frozen into place, allowing the tip to remain in contact with the ice during the first 2–4 mm of retreat. See Figure 3.2 a) for a close-up of thermocouple positioning. The wire is 36-gauge and has a negligible spring force to affect the load-cell reading. It is assumed that the vapor at the surface of the ice is saturated with respect to water vapor. The temperature thus measured gives the saturation vapor pressure at the surface of the ice via the ITS-90 formulation for vapor pressure

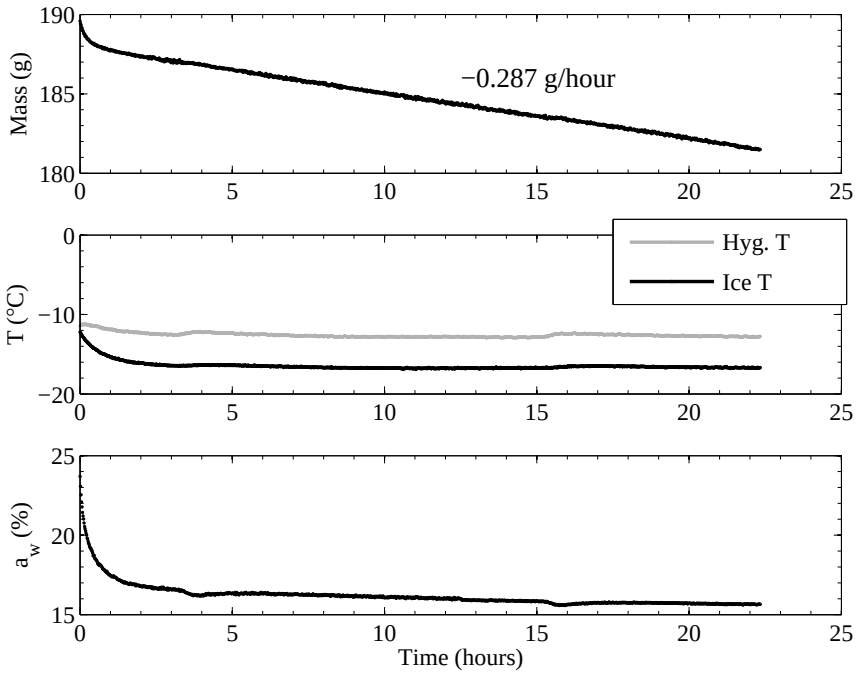

Figure 3.3: Data for a single sample: February 17, 2006. Conditions: 40 μm glass beads, 2 cm thick, T $\approx$ 263 K. The mass loss rate displayed in the top axis is determined from a linear regression to post-transient data.

(*Hardy*, 1998). Figure 3.3 shows ice surface temperature as a function of time for one experiment.

The RH/RTD sensors simultaneously report water activity, a_w, and ambient temperature at the sensor. Figure 3.2 c) shows examples of placement and Figure 3.3 shows the data as reported. Capacitive sensors such as the HIH-3602 are responsive to water activity rather than to relative humidity (*Anderson*, 1995; *Koop*, 2002). The difference is that water activity is the ratio of vapor content of the atmosphere p_1 to the saturation vapor pressure over liquid water, $p_{\rm sv}^{\rm liq}$, rather than over ice:

$$a_w = p_1/p_{\rm sv}^{\rm liq}. \tag{3.1}$$

Thus the true relative humidity is given by:

$$RH = p_1/p_{\rm sv}^{\rm ice} = a_w p_{\rm sv}^{\rm liq}/p_{\rm sv}^{\rm ice}. \tag{3.2}$$

The equation for $p_{\rm sv}^{\rm liq}$ is determined from data on supercooled water taken from *Hare and Sorensen* (1987). The ITS-90 formulation is used for $p_{\rm sv}^{\rm ice}$ to determine RH, and then used again to convert the relative humidity calculated above the sample into a partial pressure of water via the ideal gas law.

3.3 Materials

The martian regolith is a complex substance. Early lander-based measurements of elemental composition show close similarity among widely spaced sites (*Arvidson et al.*, 1989). Despite discoveries by both Viking and the MER mission that reveal significant chemical and physical differences among the non-rocky components of the surface (*Moore et al.*, 1979), they are very similar in absolute terms over planetary-scale distances. Various investigators have used the JSC Mars–1 palagonite ash from Mauna Kea to simulate Mars regolith in a variety of experiments (*Gilmore et al.*, 2004; *Cooper and Mustard*, 2002; *Gross et al.*, 2001). Martian soils no doubt come in a variety of grain size distributions, grain shapes, porosities, compositions, and degrees of compaction and cementation. With respect to the demonstrably heterogeneous Martian regolith, the Mars–1 soil is not assumed to match a particular locality on Mars, but rather is a complex, natural soil material which may represent a general class of Mars regolith. A thorough description of JSC Mars–1 can be found in *Allen et al.* (1997, 1998).

JSC Mars–1 contains a variety of minerals which exhibit different patterns of fracture, cleavage, and surficial chemical structure making this a very complex regolith simulant. The JSC Mars–1 simulant can be easily characterized, but the parameter space to be explored is vast. Working with fine-grained granular media presents many challenges, particularly with regards to repeatability. To eliminate some of the complexities involved in studying a chemically and physically heterogeneous disaggregated mineral assemblage, some simpler and more easily handled proxies for porous regolith materials are used.

50–80 μm beads: An easily characterized and handled material used frequently in these experiments. Obtained from AGSCO Corporation, this material is composed of spherical soda lime glass (specific gravity: 2.50) beads with a narrow particle size distribution.

"Coarse" Frits: The only consolidated media used in this study, these are disks composed of sintered borosilicate glass beads (specific gravity: 2.53). These porous filter disks were obtained from ChemGlass Inc., whose catalog states that the nominal pore size for the "coarse" category of frits are between 50 and 80 μm.

1–3 μm dust: These smaller particles act as a proxy for Mars airborne dust. Obtained from Powder Technology, Inc., under the trade name "Arizona Test Dust", this is a natural silicate mineral with a specific gravity of 2.65. It exhibits a narrow particle size range of equant yet angular particles.

JSC Mars–1: Weathered palagonitic ash from Pu'u Nene cinder cone, Hawai'i. This natural basaltic mineral assemblage has a wide particle size distribution from 1 mm down to < 1 μm,

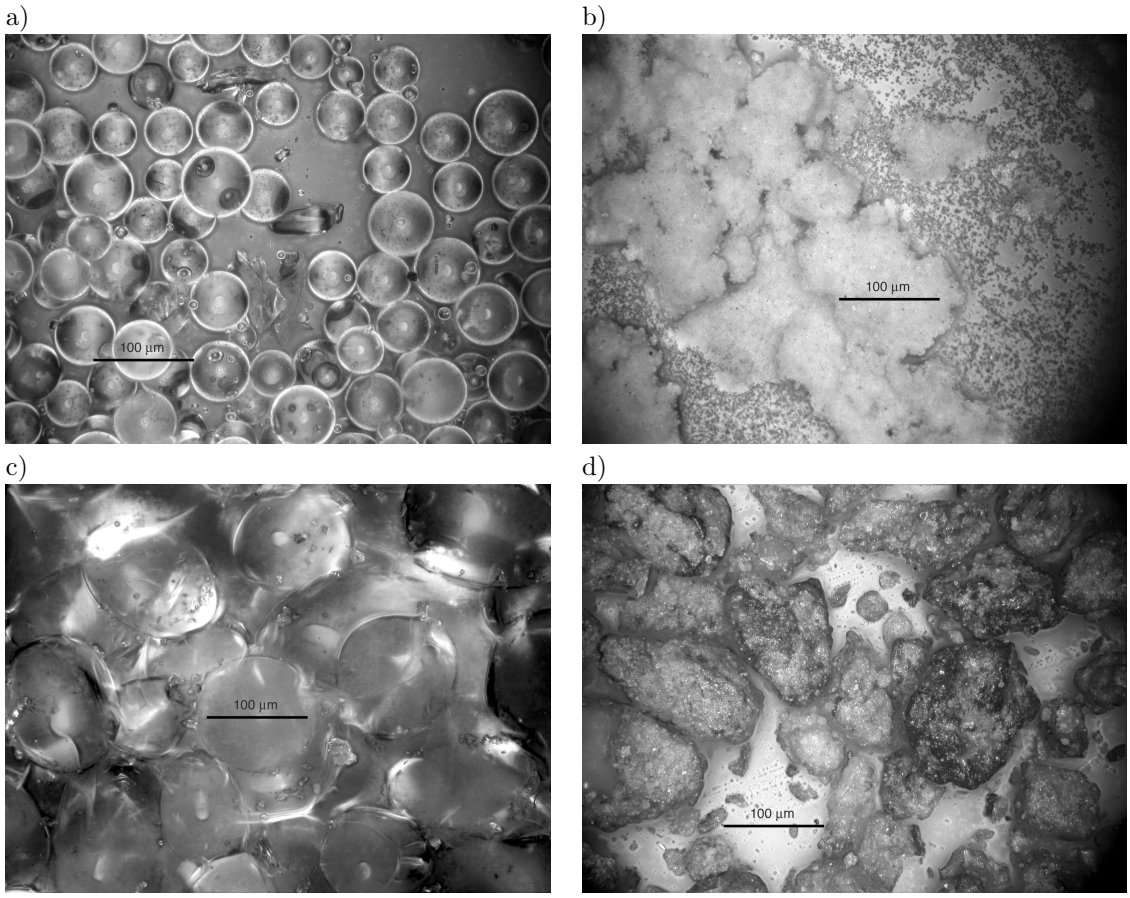

Figure 3.4: Optical micrographs of regolith simulants: a) 50–80 μm beads, b) 1–3 μm Arizona Test Dust (note the presence of aggregates), c) "Coarse" fritted disks, pore size 50–80 μm, and d) raw JSC Mars–1

and a complex overall mineralogy. The washed and sifted supply of this simulant was obtained through the Johnson Space Center Curator.

Wind-blown sand particles on Mars were proxied by the glass beads, whose size range is similar to that observed in Mars wind-tunnel experiments and at MER landing sites (see Section 3.3.1). The Arizona Test Dust approximates size characteristics of dust on Mars. The porous frits were chosen to illustrate experimental repeatability given a medium with an unchanging geometry. JSC Mars–1 was selected because it has been frequently used in other investigations of Mars analogue materials.

See Figure 3.4 for optical micrographs of these simulants at the same scale. Prior to use, all samples are dried in an oven at 383 K and then stored in air-tight containers.

Geometric porosities of the separate materials were determined by weighing a known volume of bulk sample to determine a bulk density, ρ_{bulk}, and ratioing this against the known specific gravity of the individual particles ($\phi = 1 - \rho_{\mathrm{bulk}}/\rho_{\mathrm{true}}$). The results are given in Table 3.1.

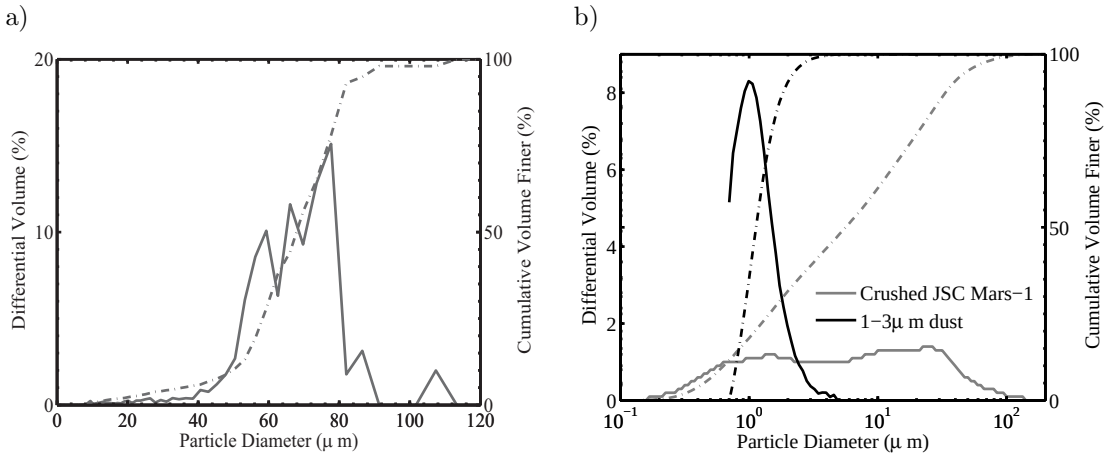

Figure 3.5: Particle-size histogram (solid) and cumulative finer (dash-dot) plots for a) 50–80 μm glass beads and b) crushed JSC Mars-1 and 1–3 μm dust

3.3.1 Glass beads

The spherical beads of soda lime glass exhibit a narrow particle size distribution between 50 and 80 microns, equivalent to the sedimentological category of "fine sand". As seen in the optical micrograph image in Figure 3.4a, the bead particles are all nearly perfect spheres. The sample was analyzed by Particle Sizing Systems using a model 780 AccuSizer with light obscuration and light scattering techniques. Ninety percent of the particles are larger than 48 μm and only 10% are larger than 80 μm. The volume-weighted mean particle size is 64.4 μm, with a median of 66.1 μm and a mode of 77.7 μm, reflecting a slight skew towards the larger diameters. The results of the analysis are shown graphically in Figure 3.5 a). At least 70% of the beads fall within the size range given, with no more than 10% being larger, no more than 20% being smaller, and no more than 3% being broken or angular in shape.

Within a factor of two in friction threshold velocity, these are similar to the 100 μm size of the most easily lofted particles under martian conditions (*Greeley et al.*, 1980). Terrestrial analogs and wind-tunnel experiments suggest that suspended dust is usually not incorporated into sand dunes, and Spirit Microscopic Imager pictures indicate that sand sheets in Gusev crater are largely composed of fine to medium sand-sized particles.

Pore sizes may be estimated from particle size. Between three coplanar spherical particles of

Simulant	ϕ, %	ρ_{bulk}, g cm^{-3}	ρ_{true}, g cm^{-3}
50–80 μm Glass Beads	42±1.0	1.46±0.5	2.50
Crushed JSC Mars-1	64±1.0	1.09±0.5	3.07
Loose 1–3 μm dust	86±0.2	0.25±0.03	2.65
Packed 1–3 μm dust	75±0.8	0.66±0.03	2.65

Table 3.1: Porosities, true densities, and bulk densities for simulant materials

the same radius, the theoretical minimum pore size is $r_{\min} = r_{\text{particles}}(3\sqrt{3}/4 - 1)$. The largest dimension between kissing points in a cubic packing of spheres is the diameter d. Between such wide openings the pore space constricts to only $d(\sqrt{2} - 1)$ when passing between one cubic unit cell to the next. Thus for a mixture of beads with 50–80 μm close-packed particles, the minimum pore size is 11.96 μm and the maximum is 80 μm. With a mean free path of $\sim$12 μm under experimental conditions, this gives a ratio of r/λ_1 from 1.0 to > 2.4, well within the transition regime between Fickian and Knudsen diffusion. Nevertheless, close-packing of spheres may not obtain throughout the sample and larger irregular pores are likely. Given the tendency for the majority of diffusive flux to be accommodated in the largest pores (*Clifford and Hillel*, 1983), it may be expected that diffusion will be dominated by Fickian processes, but that Knudsen interactions with the pore walls will also play a role.

3.3.2 Crushed JSC Mars-1 dust

JSC Mars-1 is a weathered palagonitic ash from the Pu'u Nene cinder cone on Mauna Kea, Hawai'i and has been used in a variety of Mars surface simulation experiments beyond its originally intended use as a spectral analog (*Gilmore et al.*, 2004; *Cooper and Mustard*, 2002; *Gross et al.*, 2001). The raw JSC Mars-1 was obtained through the Johnson Space Center Curator. A thorough description of JSC Mars–1 can be found in *Allen et al.* (1997, 1998).

Raw JSC Mars-1 particles were crushed to smaller sizes in a planetary ball mill. Batches of 250 mL of oven-dried raw material were run with 50 hardened steel milling balls at 590 RPM for two 10 minute cycles. The resulting particle size distribution was analyzed by Micromeritics Instrument Corporation on a Saturn DigiSizer 5200 using the laser light scattering technique. Particles were dispersed in a 0.3% Daxad 23 / 40% sucrose / water solution in an ultrasonic bath for 1–2 min. The measured median particle size is 5.46 μm. The whole distribution is bimodal with peaks at 1.5 and 25.2 μm; nearly 70% of the volume is larger than 2 μm. The volume percent and cumulative finer distributions for this simulant are shown as grey lines in Figure 3.5 b).

An average specific gravity of 1.91 for raw JSC Mars–1 as given by *Allen et al.* (1998) was quoted in *Hudson et al.* (2007). Recent analysis of the crushed sample with He gas-displacement in an AccuPyc 1330 Pycnometer at Micromeritics Instrument Corporation yielded an average particle density of 3.07 g cm^{-1}. This value is used in subsequent calculations in this paper.

3.3.3 1–3 micron dust

A fine dust with a very narrow particle size distribution, called "Arizona Test Dust" was obtained from Powder Technology Inc. The dust consists of a natural silicate material with a specific gravity of 2.65. The dust is composed of equant yet angular particles which easily form weak mm- to cm-

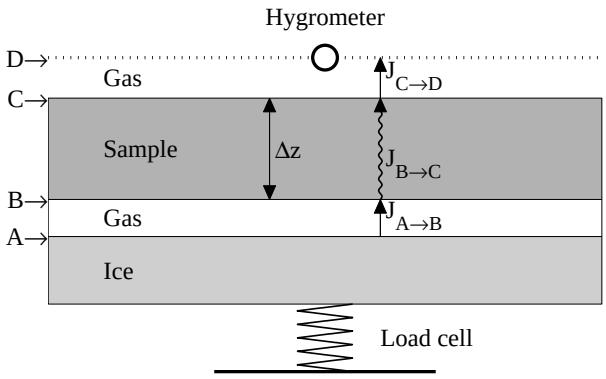

Figure 3.6: Generalized schematic of experimental setup showing gas gaps separating both the ice surface and hygrometer (RTD/RH chip) from the sample. By continuity, the vapor flux through the sample is the same as that through the gaps.

sized aggregates. Sieving breaks up these aggregates, but they easily reform under agitation or self compaction. Loose, aggregated dust alone has a calculated geometric porosity of $88 \pm 1\%$, while compressional packing results in a reduced porosity of $76 \pm 2\%$.

The particle size data for this sample, measured on a Coulter Multisizer, were provided by the manufacturer. The mean particle size is 1.19 ± 0.49 μm. The median is 1.132 μm, with less than 1.5 % of the volume in particles larger than 3 μm. The volume percent and cumulative finer distributions for this simulant are shown as black lines in Figure 3.5 b).

3.4 Analysis

This section details the procedure for reducing data from each experiment into diffusion coefficients. Figure 3.6 is a schematic drawing of the experimental setup with different levels in the sample column labeled A through D. Although unconsolidated samples always rest directly on the ice, the schematic is generalized to allow for a gap between positions A and B. A formalism to determine a correction term to account for gas gaps, sublimation effects, and true sample thickness is described below. An analysis method for the diffusion regime and pressure dependence of the diffusion coefficient is also presented.

3.4.1 Determining the diffusion coefficient

Equation (2.4) is valid in the limit where the mass concentration of H_2O, c, and therefore advection, is small, and it is used to extract the diffusion coefficient from measurements above (position "D" in Figure 3.6) and below (position "A" in Figure 3.6) the soil sample:

$$J_1 = D' \frac{\rho_{1\mathrm{A}} - \rho_{1\mathrm{D}}}{\Delta z}, \tag{3.3}$$

where D' is the "raw" diffusion coefficient. The vapor density above the sample $\rho_{1\mathrm{D}}$ is determined from measurements of temperature and humidity in the air which gives a partial pressure of water vapor $p_{1\mathrm{D}}$, and thereby $\rho_{1\mathrm{D}} = p_{1\mathrm{D}} M_1 / RT_{\mathrm{D}}$. Vapor density at the ice surface is calculated from the saturation vapor pressure determined from the measured ice temperature, $\rho_{1\mathrm{A}} = p_{sv}^{\mathrm{ice}} M_1 / RT_{\mathrm{A}}$.

3.4.2 Correcting the diffusion coefficient

When vapor is not diffusing through a porous medium it may still encounter resistance. To undergo gas-phase transport, H_2O molecules must first sublime from the ice surface into vapor. This vapor must then diffuse through a boundary layer and any intervening gas between the ice and sample surfaces. After passing through the sample, this vapor must pass from the sample surface to the hygrometer. These gas layers may not be well mixed, resulting in an underestimated diffusion coefficient. Additionally, the measured thickness of the samples is only from B to C, not from A to D. The diffusion coefficient defined in equation (3.3) is therefore referred to as the raw diffusion coefficient. A correction to the raw diffusion coefficient for the effects of sample thickness, sublimation effects, and gas gaps may be performed given sufficient data.

By conservation of mass, the flux of vapor is the same through all three barriers $J_{\mathrm{A}\to\mathrm{B}} = J_{\mathrm{B}\to\mathrm{C}} = J_{\mathrm{C}\to\mathrm{D}} \equiv J_1$ (see Figure 3.6). Assuming that the fluxes between A and B and between C and D are still proportional to the density gradient, $J_1 = J_{\mathrm{A}\to\mathrm{B}}$ can be used to determine $\rho_{1\mathrm{B}}$ and $J_1 = J_{\mathrm{C}\to\mathrm{D}}$ can be used to determine $\rho_{1\mathrm{C}}$, while $\rho_{1\mathrm{A}}$ and $\rho_{1\mathrm{D}}$ are measured. Substituting these into an expression analogous to equation (3.3) and simplifying, the resulting corrected expression for the diffusion coefficient in the sample is

$$J_1 = D\frac{\rho_{1\mathrm{B}} - \rho_{1\mathrm{C}}}{\Delta z} = D\frac{\rho_{1\mathrm{A}} - \rho_{1\mathrm{D}}}{\Delta z + z_{\mathrm{corr}}}. \tag{3.4}$$

The quantity z_{corr} has units of length and accounts for effects other than diffusion through the porous medium including gas-gas diffusion in gaps above and below the sample and any sublimation limitation.

The correction term z_{corr} can be determined if several measurements of identical samples with different thicknesses are available. By recasting the corrected expression, equation (3.4), as linear in terms of sample thickness, Δz,

$$\frac{\Delta\rho_1}{J_1} = -\frac{\Delta z}{D} - \frac{z_{\mathrm{corr}}}{D}, \tag{3.5}$$

a linear fit can be performed and the constants z_{corr}/D and $1/D$ determined by the intercept and slope, respectively. The same correction term should apply to all experiments with the same temperature, pressure, and sample type. The term z_{corr} may now be used with the right-hand-side of equation (3.4) to solve for corrected individual values of D. Since the total vapor density gradient

is smaller for thinner samples, the relative contribution of the gas gap is larger and the necessary correction $1/(\Delta z + z_{\mathrm{corr}})$ will likewise be larger. At some thickness, the ratio of gas layer resistance to porous medium resistance will be comparable to the systematic errors in the experimental method. For example, it was found that for glass beads, the effect of the correction term became negligible for samples greater than either 2 or 5 cm thick.

3.4.3 Diffusion regime

At intermediate pressures when both collisions with other molecules and with the pore walls are important, the diffusion is said to be in transition between the Fickian and Knudsen regimes. The Bosanquet interpolation derived in equation (2.15) says that the effective diffusion coefficient D is made up of contributions from both a pressure-dependent Fickian diffusion term and a Knudsen term:

$$\frac{1}{D(p_0)} = \frac{p_0}{p_{\mathrm{ref}} D_{\mathrm{F}}(p_{\mathrm{ref}})} + \frac{1}{D_{\mathrm{K}}}, \tag{3.6}$$

where we have explicitly written the pressure dependence of the Fickian term in terms of the value of D_{F} at a particular reference pressure, p_{ref}. Substituting equation (3.6) into (3.3) produces the complete expression for flux in terms of pressure and two diffusion coefficients:

$$J_1 = \frac{1}{\frac{p_0}{p_{\mathrm{ref}} D_{\mathrm{F}}(p_{\mathrm{ref}})} + \frac{1}{D_{\mathrm{K}}}} \frac{\rho_{1\mathrm{A}} - \rho_{1\mathrm{D}}}{\Delta z}. \tag{3.7}$$

If data is taken at a number of different pressures, the parameters $D_{\mathrm{F}}(p_{\mathrm{ref}})$ and D_{K} may be fit to the flux data.

3.5 Results

Presented here are the first diffusion coefficients measured for unconsolidated porous media under simultaneous conditions of low pressure and temperature appropriate to Mars surface and shallow-subsurface studies. Four simulant materials are considered, with the largest data set being for 50–80 μm beads. Limited investigations were also performed on three other simulant materials: porous glass filter disks (frits), JSC Mars–1, and 1–3 μm dust.

3.5.1 50–80 μm glass beads at 260 K

Experiments were run for several thicknesses and a regression was calculated to determine the correction term, z_{corr}, as described in Section 3.4.2. The correction term is found to be 0.58 ± 0.07 cm. The raw and corrected diffusion coefficients are plotted in Figure 3.7. The uncorrected diffusion coefficient is moderately correlated with sample thickness (R = 0.57). Applying the correction term

$z_{\rm corr}$ to the calculation of D nearly eliminates the correlation (R = -0.02).

The weighted mean of the corrected diffusion coefficients is 4.49 cm^2 s^{-1}, with a weighted standard deviation of 0.69 cm^2 s^{-1}. Raw values from 5 and 10 cm samples are indistinguishable from this range. If the dependence of diffusion coefficient on temperature of $T^{3/2}$ as appropriate for a hard elastic sphere model of Fickian diffusion is used, the value of D at a typical Mars temperature of 200 K is 3.06 ± 0.47 cm^2 s^{-1}.

For the diffusion coefficient of a free gas scaled to the the appropriate temperatures and pressures, the formula given by *Wallace and Sagan* (1979) is used, with a 6% error to account for differences between this and other calculations of $\mathcal{D}_{12}$. For conditions of 600 Pa and 260 K, the calculated $\mathcal{D}_{12}$ is 26.4 ± 0.7 cm^2 s^{-1}.

Experiments were conducted on columns of loose glass beads with thicknesses of 1 and 10 cm under an N_2 rather than CO_2 atmosphere. A correction term of 0.70 ± 0.14 cm was calculated and applied to these samples. The corrected diffusion coefficient determined under a CO_2 atmosphere is 4.62 cm^2 s^{-1} for 10 cm columns, while the same quantity for N_2 is 5.25 cm^2 s^{-1}. According to equation (2.7) the diffusion coefficient in N_2 should be larger than in CO_2 by a factor of approximately 1.4, *i.e.,* the ratio of $\mathcal{D}_{12}$ for H_2O in the two gases as determined using the expression of Holman in Section 2.3. The difference observed is a factor of 1.14. Though somewhat smaller than expected, the change in diffusion coefficients is of the right magnitude and direction. The agreement between obstruction factors in glass beads under different host gases but similar conditions of temperature and pressure validates the data analysis method.

3.5.1.1 *Errors and scatter*

Formal errors in the diffusion coefficient are calculated by taking partial derivatives of equation (3.4) with respect to five measurable quantities: z, $z_{\rm corr}$, J_1, $\rho_{1\rm A}$, and $\rho_{1\rm D}$. Each contributing partial is then sum-squared to give the total error in D. Flux error derives from mass loss errors, which are the standard deviations of all post-transient data points with respect to the linear regression. Error in sample thickness is estimated as a ± 1 mm measurement error in all cases.

Though ideally constant throughout a particular experiment, humidities, total pressures, and temperatures do exhibit some degree of time variation. Errors in $\rho_{1\rm D}$ and $\rho_{1\rm A}$ are taken from contributing errors in $T_{\rm ice}$, $T_{\rm air}$, RH, and p_0. Experiments with multiple thermocouples show variations in $T_{\rm ice}$ on the order of 0.4 K from the sample edge to its center. The error, $\mathrm{d}T_{\rm ice}$, is the greater of the standard deviation of the measurement of $T_{\rm ice}$ and 0.4 K. The error is no greater than 0.46 K for any experiment. The error in saturation vapor pressure at the ice surface is the difference between the saturation vapor pressures calculated at $T_{\rm ice} + \mathrm{dT_{ice}}$ and $T_{\rm ice} - \mathrm{dT_{ice}}$, making the error in p_{H_2O} at the ice surface a conservative overestimate. Errors in the quantities $T_{\rm air}$, RH, and p_0 are taken as the standard deviation of logged data points.

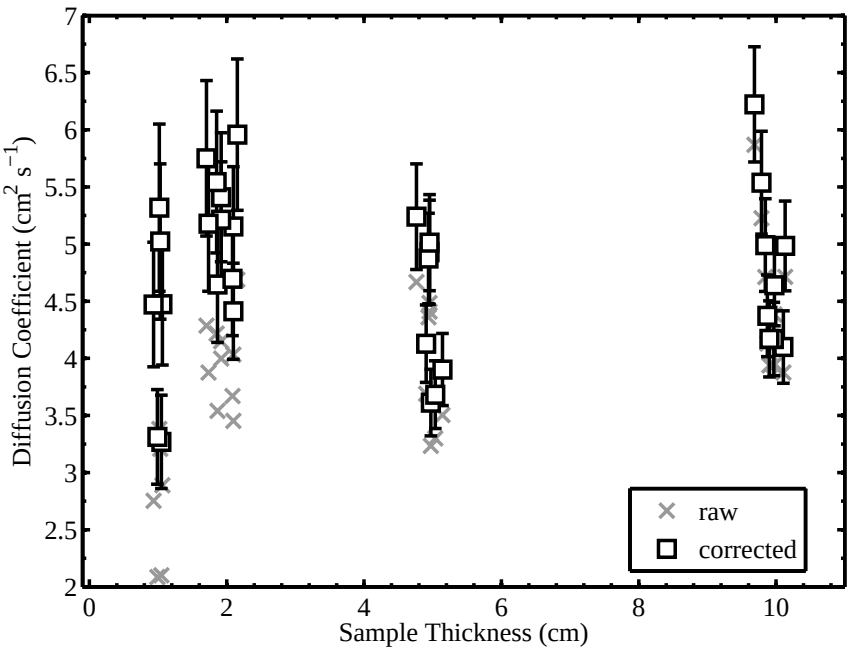

Figure 3.7: Measured and corrected diffusion coefficients for 50–80 μm glass beads at 263 K and 600 Pa. The influence of boundary layer diffusion decreases as the sample thickness (*i.e.,* resistance) increases. The correlations between D' (raw data) and thickness are 0.57, but only -0.02 between D (corrected data) and thickness.

Less than 2% of the error in the value of D for each experiment comes from z_{corr}, J_1, and $\rho_{1\mathrm{D}}$. The dominant errors are those in z and $\rho_{1\mathrm{A}}$, which range from 1–8% of the value of D. For all experiments the combined error is less than the value of D by a factor of ten or more.

The greatest uncertainty in D comes from systematic variation between experimental runs. Variations in input parameters to the diffusion coefficient such as thickness, relative humidity, temperature, pressure, and flux should be accounted for by the calculations since the expressions for D explicitly or implicitly include these parameters. Scatter may therefore arise for two reasons.

First, effects arising from advection, gas composition, and barodiffusion could contribute to each experimental run a flux unaccounted for in the described methodology. As stated above, the maximum contribution of any of these individual effects is expected to be no greater than 10%. Barodiffusion could contribute to each experimental run a flux unaccounted for in the described methodology. As stated above, the maximum contribution of any of these individual effects is expected to be no greater than 10%.

Second, there may be errors arising from changes in the experimental setup itself. The largest variation in measured quantities among samples of a given thickness is in relative humidity, which may vary by between 25–48% among individual experiments. Repositioning or substituting sample vessels may affect the flow of gases in the overturning chamber atmosphere. Water vapor densities at the surface of the sample may not be uniform in the horizontal or vertical directions and the

relative humidity measured by the hygrometer may not reflect the average environment across the the sample surface.

Numerous experiments have been run in many identical conditions, allowing confident bounds on measured diffusion coefficients to be given, though in some cases apparent outliers still have a discernible effect on the averages.

3.5.1.2 *Variable pressure experiments*

Experiments were performed at 300, 600, 1200, 3000, and 6000 Pa using a 5 cm column of 50–80 μm beads. Measurements at many thicknesses for each pressure are unavailable, so a correction term is not applied to the variable pressure data. It is not assumed that the correction term for glass beads is the same at all pressures, but it is assumed that 5 cm is enough thickness to make the correction contribution small at all pressures measured. Pressures less than $\sim$250 Pa were not used; at these lower pressures the vapor pressure of the ice becomes a significant fraction of the total chamber pressure and the experiment is no longer in a predominantly diffusive mode. A non-linear least-squares fit calculated using the method in Section 3.4.3 is compared to calculated (uncorrected) diffusion coefficients in Figure 3.8.

The fit parameters thus determined are $D_F(p_0) = 6.5\ (600\ \mathrm{Pa}/p_0)\ \mathrm{cm}^2\ \mathrm{s}^{-1}$ and $D_K = 9.8\ \mathrm{cm}^2\ \mathrm{s}^{-1}$ and are shown as solid lines in Figure 3.8. The transition pressure, where $D_F(p_0) = D_K$ is found to be at 398 Pa. The transition pressure corresponds to a mean free path of 18 μm, which is near the smaller end of the estimated pore size distribution. Mars surface pressures fall between the extremes measured, and are quite close to the transition pressure, placing materials of similar porosity and tortuosity to the 50–80 μm simulant in the transition regime.

At the beginning of this subsection, experiments performed at 600 Pa, with a mean free path of $\sim$12 μm, were shown to be within the diffusion transition regime. If the pressure is increased to 1200 Pa, the mean free path is only 5.9 μm, placing the largest pores within the Fickian regime; further increase to 5700 Pa should guarantee Fickian diffusion. Conversely, diffusive transport at 50 Pa would bring the smallest pores into pure Knudsen flow, but the bulk of the sample would still be in transition.

3.5.1.3 *Porosity and tortuosity*

The measured sample masses and their volumes are ratioed to determine a bulk density. Dividing by the true density of the component materials (2.5 g cm^{-3} in the case of glass beads) results in a geometric porosity. The porosity calculated may be an overestimate if some pore spaces are unavailable for gas transport. The range of porosities calculated for the 50–80 μm beads is $44 \pm 2\%$.

The six high-pressure experiments with $p_0 = 5890$ Pa should fall within the Fickian diffusion regime. The theoretically calculated free-gas diffusion at this pressure is $2.67 \pm 0.2\ \mathrm{cm}^2\ \mathrm{s}^{-1}$. The fit

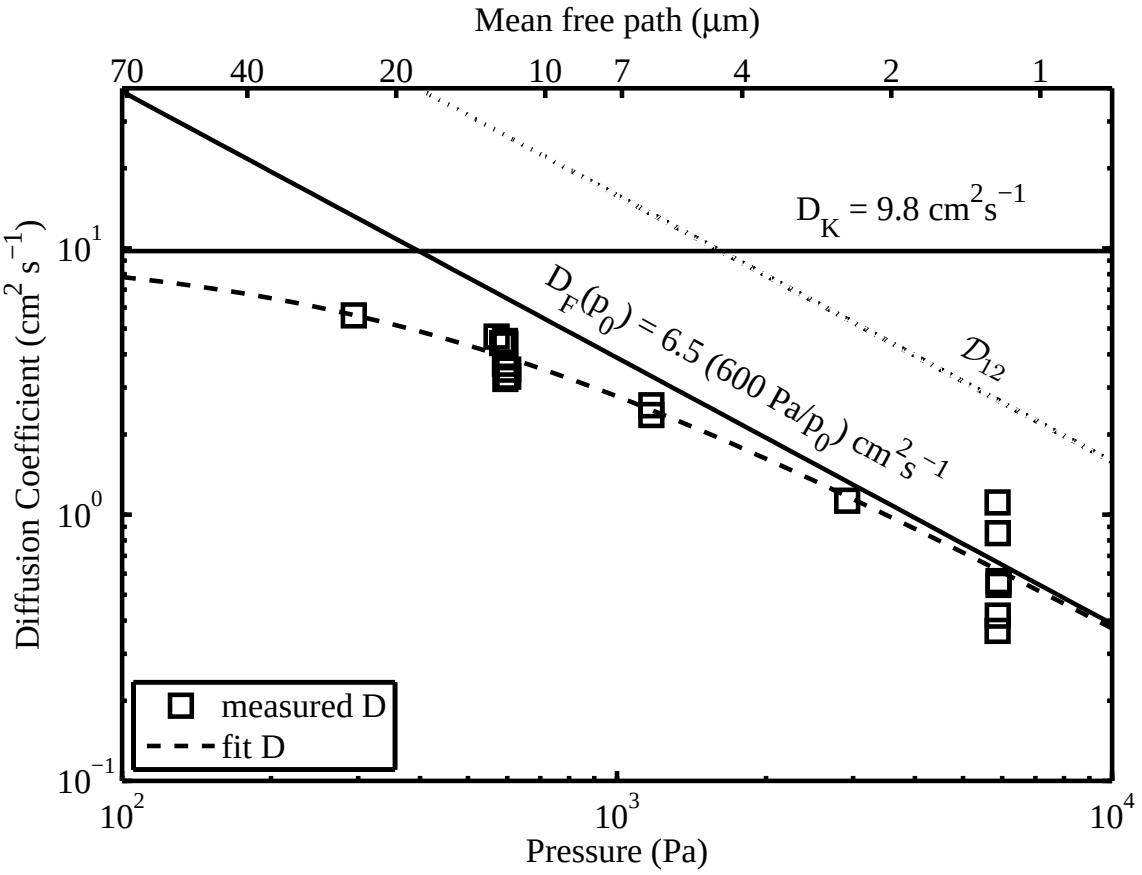

Figure 3.8: Diffusion coefficients versus pressure for 5 cm samples of 50–80 μm beads. Errors in D are smaller than the symbols. The diffusion coefficients obtained from equation (3.3) are plotted along with the fitted parameters $D_{\mathrm{F}}(p_0)$ and D_{K} (solid lines) and their interpolation D (dashed line). $\mathcal{D}_{12}$ is the free-gas diffusion coefficient as given by the expression of *Wallace and Sagan* (1979) (dotted line).

in Section 3.5.1.2 given a Fickian diffusion coefficient at 5890 Pa of 0.66 cm^2 s^{-1}. The obstruction factor is thus 0.25 ± 0.02. Using estimates for geometric porosity, equation (2.3) may be used to calculate a tortuosity $\tau = 1.7 \pm 0.6$. Using the raw data for each experiment instead of the fitted D_{F}, the weighted mean and standard deviation of the diffusion coefficient for the high-pressure experiments is 0.49 ± 0.18 cm^2 s^{-1}. With the same value of $\mathcal{D}_{12}$ given above, the obstruction factor $D/\mathcal{D}_{12} = \phi/\tau = 0.18 \pm 0.07$ and the tortuosity factor is $\tau = 1.5 \pm 0.6$.

Equation (2.3) is true for Fickian diffusion and is therefore appropriately applied to data taken at higher pressures. If this expression is used with values of D obtained at ~600 Pa, the value of the tortuosity obtained is $\tau = 2.4 \pm 0.3$. This is an overestimate of the tortuosity because the data are in the transition regime (see Figure 3.8) and include a component of Knudsen diffusion.

A distinction must be drawn between tortuosity and the tortuosity factor. As reviewed by *Epstein* (1989), "tortuosity" refers directly to the ratio of the pore path length L_e to the length of

the porous medium along the major flow or diffusion axis L. However in calculating the effective diffusion coefficient using a parallel-pore conceptual model, a second factor of L_e/L enters the expression because of the increase in capillary velocity over the axial velocity (along L) when there is no divergence of the flow. Thus the factor of τ presented herein is the "tortuosity factor", equal to $(L_e/L)^2$. The methods using either high-pressure data or (equivalently) the fitted Fickian diffusion coefficient give an increase in pore path length over sample length, L_e/L, of 1.3, while the overestimate made with individually determined values of D gives $L_e/L = 1.6$.

At lower pressures, as diffusion begins to transition into the Knudsen regime, D ceases to depend on pressure through $\mathcal{D}_{12}$ and the obstruction factor may be written with additional factors as shown in equations (2.11) and (2.12). In the formalism used by *Evans et al.* (1961), the τ in these equations is the same as the τ in equation (2.3). Equation (2.13) can be used to determine that the value of τ above will correspond to the fit value of $D_K = 9.8$ cm^{2}s^{-1} if the value of $\bar{r}$ for glass beads is 14.4 μm. This is only slightly larger than the theoretical minimum pore space of 11.96 μm, suggesting that the sample is near closest-packing and that few pathways much larger than $\sim$40 μm are available for diffusion. Calculated obstruction factors ($D/\mathcal{D}_{12}$) for glass beads range between 0.12 and 0.23 except for two outliers at 0.35 and 0.46 measured at high pressures. The majority are within the range of obstruction factors given by *Currie* (1960) for closest packing (0.13) to cubic packing (0.38) of spherical particles.

Mechanical packing (tamping, shaking, or pressing) of this sample does not measurably reduce porosity, and neither porosity, tortuosity nor their ratio correlate strongly with mass loss rate or the free-gas diffusion coefficient. There are no apparent correlations between quantities that should be independent, indicating that the above method of determining tortuosity is not systematically offset.

The data for water vapor fluxes show a greater spread in values for the thinner samples. A major factor which may contribute to the reduction in scatter with thickness is the averaging of pore geometry along the sample. The loose glass beads have a mean diameter of $\sim$55 μm. The measured obstruction factors suggest packing densities between hexagonally close-packed and cubic-packed, implying that there are between 180 and 230 layers of particles per centimeter. For thicker samples, the properties of the medium can average out and present smaller variations between experiments. Additionally, large voids occurring as a result of random packing will offer a very efficient path of vapor transport which could significantly impact the sample diffusivity. Such voids would be a smaller proportion of the total length for thicker samples, thus offering fewer wide, connected paths from the ice to the surface.

3.5.1.4 *Water contents*

Following each diffusion experiment, samples were weighed, baked in an oven at 383 K for >12 hours, and weighed again to gravimetrically determine water contents (per ASTM test method D2216). The weighing techniques employed allowed the determination of mass differences to within ±1 g. For 50–80 μm glass beads, the difference between pre- and post-bake masses was never more than this detection limit except for experiments with 10 cm samples. These large samples never exhibited more than 3 grams of difference, which corresponds to a maximum 6 mg g^{-1} of water content.

At the end of experiments involving 5 and 10 cm sample columns, the bottom 2 cm of sample exhibited mild cohesion while the upper portions of the sample showed none. This suggests that the water content would be relatively higher at the base of the sample if it were measured independently. Such a non-uniform distribution of adsorbed water could reflect the vapor gradient along the sample length. A higher partial pressure near the bottom would cause a larger degree of adsorption there and some threshold water content for cohesion may be reached.

The strongly linear behavior of the mass-loss curves following the initial thermal transients suggests that the absorptive capacity of the samples is filled in less than the transient time. This rate is much faster than would be obtained given only the ice retreat rates in the post-transient interval. It is likely that higher vapor pressures in thermal transient phase, vapor pumping from the ice during evacuation of the chamber, or absorption from the relatively moist freezer atmosphere acts to fill absorptive sites quickly. See the discussion of adsorption below (Section 3.6.1) for more detail on the steady-state nature of these experiments.

3.5.1.5 *Other effects*

If the transition rate from ice into vapor is comparable to the diffusive flux, this sublimation rate will limit the flux measured. For a given ice temperature, the total flux would be independent of the sample thickness if the flux were sublimation-rate limited. For such a constant flux, D would be observed to increase with sample thickness. This is observed in the uncorrected samples, though the effect may be due also to gas diffusion in the gaps above and below the porous medium. The correction term removes both effects simultaneously and since $z_{\mathrm{corr}} < z$, the sublimation limit correction is known to be small. Direct measurements of vapor density at the hygrometer, total flux, and the assumption of a saturated atmosphere below the sample produces valid data.

Sublimation carries away the latent heat of the subliming ice (2,845 kJ kg^{-1} at 273 K), cooling the sample surface. Multiple thermocouples embedded in the ice block during experiments both with and without a diffusive barrier show that temperature variations in the ice block are small. The maximum measured temperature difference across the 1 cm block (no cover, free ice) is no more than 0.8 K; the top surface near the caddy wall being the warmest spot. The ice (thermal conductivity:

2.2 W m^{-1} K^{-1}) therefore requires a heat input of approximately 180 W/m^2. Thermocouples near but not in contact with the a free ice surface record an atmospheric temperature of ∼255 K, which falls between that of the embedded thermocouples (∼250 K) and the RTD temperature element in the hygrometer (∼260 K). The apparent primary heat input to the ice is thus the warmer chamber atmosphere. When the ice is uncovered, this heat reaches it most effectively through convection. When a sample overlies the ice, heat is conducted through the diffusive barrier. Under a chamber atmosphere of 261 ± 0.6 K, the ice temperatures measured for 1, 5, and 10 cm are 256.1 K, 259.3 K, and 260.1 K, respectively. This shows that the thicker samples have heat inputs similar to the thin-sample cases, but their diffusive resistance allows less efficient cooling through sublimation.

3.5.2 50–80 μm glass beads at 253 K

Several experiments have been run on the 50–80 μm beads at reduced temperatures to take advantage of lower advective fluxes when saturation vapor pressures over ice are smaller (see equation (2.22)). A paucity of data points and a small spread of sample thicknesses prevent the calculation of a correction term; the data presented are the raw diffusion coefficients. The diffusion coefficient is found to be 4.21 ± 0.65 cm^2 s^{-1}, slightly lower than the value determined for samples run at 263 K, but indistinguishable within the range of systematic scatter. Extrapolation to 200 K results in $D = 3.03 \pm 0.47$ cm^2 s^{-1}, nearly identical to the extrapolation of the 263 K value of D. The free-gas diffusion coefficient at 253 K is ∼5% lower than $\mathcal{D}_{12}$ at 263 K. The calculated obstruction factor at 253 K is virtually identical to that determined at 263 K, and the tortuosity is likewise similar: $\tau = 2.4 \pm 0.4$.

3.5.3 Glass frits

To check the degree of systematic variation in the experimental setup, a series of experiments were performed with porous glass filter disks, or "frits". Stacks of frits with a nominal pore size of 80 μm were assembled with electrical tape into columns of 1–8 frits (∼0.5 to ∼5 cm) which were then fastened with tape onto caddies full of ice. The distance between the ice and the frits at the start of the experiments was less than 1 mm.

The calculated correction term z_{corr} was approximately zero and was therefore neglected. The diffusion coefficient determined, 2.80 ± 0.22 cm^2 s^{-1}, is about a factor of 1.6 lower than that measured for the unconsolidated 50–80 μm beads. As expected, the porous frits exhibit a lower degree of systematic scatter compared with that in the data for unconsolidated media. The uncertainty in the diffusion coefficients for the frits is ∼6%, while that for the glass beads is ∼16%.

The calculated porosity of the frits is $42 \pm 2\%$, indistinguishable from that of glass beads. Hence the lower diffusivity can be attributed to a more tortuous geometry of the sintered glass. The

calculated values of τ for the frits is 3.9 ± 0.4. This higher tortuosity may arise from the high temperatures and pressures of the sintering process; some of the large pore spaces which could occur in randomly packed and unconsolidated material are eliminated.

Though expected to be small (see the end of Section 2.6.3), the possible presence of gravity-dependent effects such as buoyancy were checked using an inverted experiment. Two sets of frits were run as usual for several hours. Then the chamber was opened and one set was inverted, with a gap allowing free gas flow at the sample surface above the load cell. The difference between the two runs of the inverted sample was 1.9%, while the difference between the two runs of the unaltered set was 3.1%, showing that systematic differences in the experiment exceed any measurable gravity effect on mass loss. The expected gravity-dependent effect is small as discussed in Section 2.6.3.

3.5.4 JSC Mars–1

JSC Mars–1 is the <1 mm fraction of weathered volcanic ash from the Pu'u Nene cinder cone, Hawai'i. The grains are composed of feldspar and Ti-magnetite, with minor olivine, pyroxene and glass. *Allen et al.* (1998) gives an average particle density of 1.91 ± 0.02 g cm^{-3}, but see Section 3.3.2. The uncompacted porosity is reported as 54%, decreaseable to 44% upon vibration(*Allen et al.*, 1997). Much of the mass of JSC Mars–1 is in particles larger than 149 μm, but there is a significant fraction of particles smaller than 5 μm. See the micrograph in Figure 3.4d for representative particle shapes for the raw (*i.e.,* uncrushed) material. Compared to the 50–80 μm glass beads, JSC Mars–1 has larger, more angular particles and a significant fraction of void-filling fines. However, the size and frequency of these fines is small and is not sufficient to block a significant fraction of the available pore space (*Allen et al.*, 1997).

The measured porosity is $58 \pm 2\%$, significantly larger than that determined for glass beads ($44 \pm 2\%$). This is due to the highly angular nature of the JSC Mars–1 particles; the interlocking jagged edges allow a more inflated structure to be stable against compaction. Thus, it is difficult to make estimations of the maximum and minimum pore sizes in the material. Pores larger than the largest particles would tend to form easily, but may just as often be filled with smaller material.

Unlike all other simulants, the JSC Mars–1 exhibits a pronounced decrease in raw diffusion coefficients with thickness. This is opposite the expected trend which would arise from the effects discussed in Section 3.4.2. It may be that the wide grain size distribution results in significant packing effects which give rise to smaller true diffusivities for thicker samples. The measured diffusion coefficient for JSC Mars–1 is 5.36 ± 0.72 cm^2 s^{-1}, slightly larger than the corrected value for glass beads, yet still within the range of uncertainties. The obstruction factor, 0.21 ± 0.03, is larger than the obstruction factor for glass beads, and the Fickian tortuosity $\tau = 2.6 \pm 0.4$ is slightly higher. Higher tortuosity may be a consequence of the wider particle size distribution and angular particle shapes which give rise to a more convoluted flow geometry.

A significant difference between the JSC Mars–1 and both glass beads and borosilicate frits is the amount of water retained during the course of an experiment. Approximately 10 g of water (69 mg g^{-1}) was retained at the end of an experiment with a 5 cm column of JSC Mars–1. Phyllosilicates, which could accommodate water in interlayer spaces, amount to less than 1% of the mass of the sample. More significant are small particles of weathered ash minerals including palagonite, glass, and nanophase ferric oxides which are abundant and contribute greatly to the specific surface area. The larger fraction of small particles in this simulant than in either of the other two presents a higher available surface capable of holding onto a larger amount of water.

3.5.5 1–3 micron dust

The mean particle size of the Arizona dust is 1.19 μm with a standard deviation of only 0.49 μm. The dust easily forms weak mm to cm sized aggregates that may be broken up by sieving, although they reform upon settling or mechanical agitation. Pore sizes in uncompacted samples emplaced by mechanical pouring are therefore expected to be bimodal, with a peak at small sizes ($\sim$2 μm) occurring within the aggregates, and a second, broad peak for inter-aggregate pores at sizes much larger than in any of the other simulants ($\sim$1 mm) (*Yu et al.*, 2003). Mechanical packing destroys the aggregates and closes up the largest pores. The loose, aggregated material has a calculated geometric porosity of $88 \pm 1\%$, while compressional packing results in a reduced porosity of $76 \pm 2\%$.

Data have not been taken at a sufficient spread of thicknesses to enable the calculation of a correction term for the 1–3 μm dust; the raw diffusion coefficients are reported. A significant difference is seen between loose and packed dust, the former being similar to the other simulants studied. The diffusion coefficient for the loose dust is 2.81 ± 1.32 cm^2 s^{-1}; the error bars are within the range of 50–80 μm beads and the glass frits. Packed dust exhibits a much lower diffusivity, with a mean D of 0.38 ± 0.26 cm^2 s^{-1}. One of the 2-cm-thick experiments exhibited a diffusion coefficient of 0.20 cm^2 s^{-1} while another gave a calculated D of 1.4 cm^2 s^{-1}. The small number of measurements on dust and the presence of outliers results in formal standard deviations in D and τ which are large. Further measurements are needed to refine these results and reduce the uncertainties (see Chapter 4).

A chamber pressure of 600 Pa places pores of micron size on the edge of the Knudsen regime, $r/\lambda_1 = 0.17$. The Knudsen obstruction factor may thus be defined with a quantity K_0, which depends on other factors in addition to ϕ and τ. Equations (2.11), (2.12), and (2.13) may be used to calculate a value of τ for the dust particles. Using this method, and estimating $\bar{r} = 2$ μm, the loose dust has $\tau = 5.0 \pm 1.7$, while the Fickian method (equation (2.3)) would give $\tau = 5.3 \pm 2.0$. This suggests that the loose dust behaves more like a coarser porous medium and is predominantly in the Fickian mode of diffusion. Packed dust, on the other hand, gives a tortuosity of 12.3 ± 5.1 with the Knudsen-appropriate equations, but $\tau = 23.5 \pm 10.9$ with equation (2.3). This estimate for τ depends on the

accuracy of the relationship between τ and D_K (equation (2.13)), and on the estimated average pore size. The very large values of τ seen here suggest that more quantitative methods (employing, for example, porosimetry measurements) are called for. While variable-pressure experiments were not performed on packed-dust to confirm that Knudsen diffusion was operating, the low values of diffusivity, differences between the two methods for calculating τ, and knowledge of particle size suggest that this is the appropriate regime. The small diffusivities and high tortuosities support the possibility that a thin layer of packed dust could dominate the diffusive resistance through a medium which is more open overall.

The small particles of the Arizona dust retain water well. About half as much water as the JSC Mars–1, around 34 mg g^{-1}, was retained at the end of the experiments. The dust is nearly pure silica and has no special mineralogical means of binding the water. The retained water is likely held in place through capillary action and the large surface area of the dust and dust aggregates.

3.5.6 Summary

Table 3.2 presents a summary of the data for each type of simulant.

Mass fluxes for all samples are plotted versus sample thickness in Figure 3.9. All simulants show decreasing flux at larger thicknesses. Experiments performed at 253 K, or experiments performed with packed dust, fall below the trend of other experiments. Figure 3.10 shows these fluxes as a function of temperature along with the evaporation rate curve for bare ice as given by *Ingersoll* (1970) for a dry atmosphere. Figure 3.10 also shows additional data obtained in later experiments than those described here; these will be discussed in Chapter 4.

Correction terms are applied as per Section 3.4.2 to experiments performed on glass beads at 263 K under CO_2 and N_2. The correction term determined for the glass frits is near zero and is neglected. Corrections are not applied to samples with an insufficient spread of thicknesses such as 1–3 μm dust and experiments on 50–80 μm glass beads at 253 K. A correction term is also not obtained for JSC Mars–1, which is a special case in which it is believed compaction effects result in different true diffusivities for different sample thickness.

Figure 3.11 displays the data for the simulants described in this chapter as a function of pressure; data at both temperatures ($\sim$260 K or $\sim$250 K) are included. The lines in this figure represent extrapolated free-gas diffusion coefficients using the expression of Wallace and Sagan. The trend of the variable pressure data (50–80 μm glass beads) follows this line with a constant obstruction factor of $\sim$0.18. Diffusivities for all simulants measured at 600 Pa except for packed dust fall within the range of 2.0–6.2 $cm^2\ s^{-1}$. The range of the mean values for different sample types and temperatures (but at 600 Pa only) is from 2.8 to 5.4 $cm^2\ s^{-1}$. Packed 1–3 μm dust has values of D between 0.2–1.4 $cm^2\ s^{-1}$, with a weighted mean value of 0.38 ± 0.26 $cm^2\ s^{-1}$. The obstruction factor for most simulants is between 0.09 and 0.23, while for packed dust it is 0.008–0.053. This suggests

Sample	T_{ice} [K]	D [cm^2 s^{-1}]	$D(200\ K) \propto T^{3/2}$ [cm^2 s^{-1}]	$D(200\ K) \propto T^{1/2}$ [cm^2 s^{-1}]	Porosity [%]	$\mathcal{D}_{12}$ [cm^2 s^{-1}]	$D/\mathcal{D}_{12}$	Tortuosity
50–80 μm beads	258.2 ± 1.7	4.49 ± 0.69[1]	3.06 ± 0.47	3.95 ± 0.61	44 ± 2	26.2±2.2	0.17 ± 0.03	2.4±0.3
50–80 μm beads, 6 kPa	261.2 ± 0.1	0.49 ± 0.18	0.33 ± 0.12	0.43 ± 0.16	42 ± 1	2.7±0.2	0.18 ± 0.07	1.5±0.6
50–80 μm beads, 253 K	249.4 ± 0.5	4.21 ± 0.65	3.03 ± 0.47	3.77 ± 0.58	44 ± 2	24.9±2.1	0.17 ± 0.03	2.4±0.4
50–80 μm beads, N_2	258.3 ± 1.9	5.33 ± 0.43[1]	3.63 ± 0.29	4.69 ± 0.38	43 ± 1	33.4±2.1	0.16 ± 0.01	2.6±0.2
"Coarse" glass frits	257.4 ± 1.5	2.80 ± 0.22	1.92 ± 0.15	2.47 ± 0.19	42 ± 2	26.4±2.3	0.11 ± 0.01	3.9±0.4
JSC Mars–1	257.3 ± 1.6	5.36 ± 0.72	3.67 ± 0.50	4.72 ± 0.64	58 ± 2	26.2±1.8	0.21 ± 0.03	2.6±0.4
1–3 μm dust—loose	256.2 ± 1.4	2.81 ± 1.32	1.94 ± 0.91	2.48 ± 1.17	88 ± 1	29.7±1.7	0.09 ± 0.04	5.3±1.9
1–3 μm dust—packed	260.6 ± 0.6	0.38 ± 0.26	0.25 ± 0.17	0.33 ± 0.23	76 ± 2	25.8±0.9	—	12.1±5.0[2]

Table 3.2: Summary of results for the experiments carried out at 263 K and 600 Pa in CO_2 unless otherwise noted. Weighted averages and standard deviations for T_{ice}, D, $\mathcal{D}_{12}$, $D/\mathcal{D}_{12}$, and Fickian tortuosity for all samples of a given type are listed. Diffusion coefficients are extrapolated to 200 K using $D \propto T^{3/2}$ and $D \propto T^{1/2}$ as appropriate for Fickian and Knudsen diffusion, respectively.

[1] Corrected D reported for samples for which correction data was available.

[2] Tortuosity estimated from the Knudsen diffusion coefficient and equation (2.13).

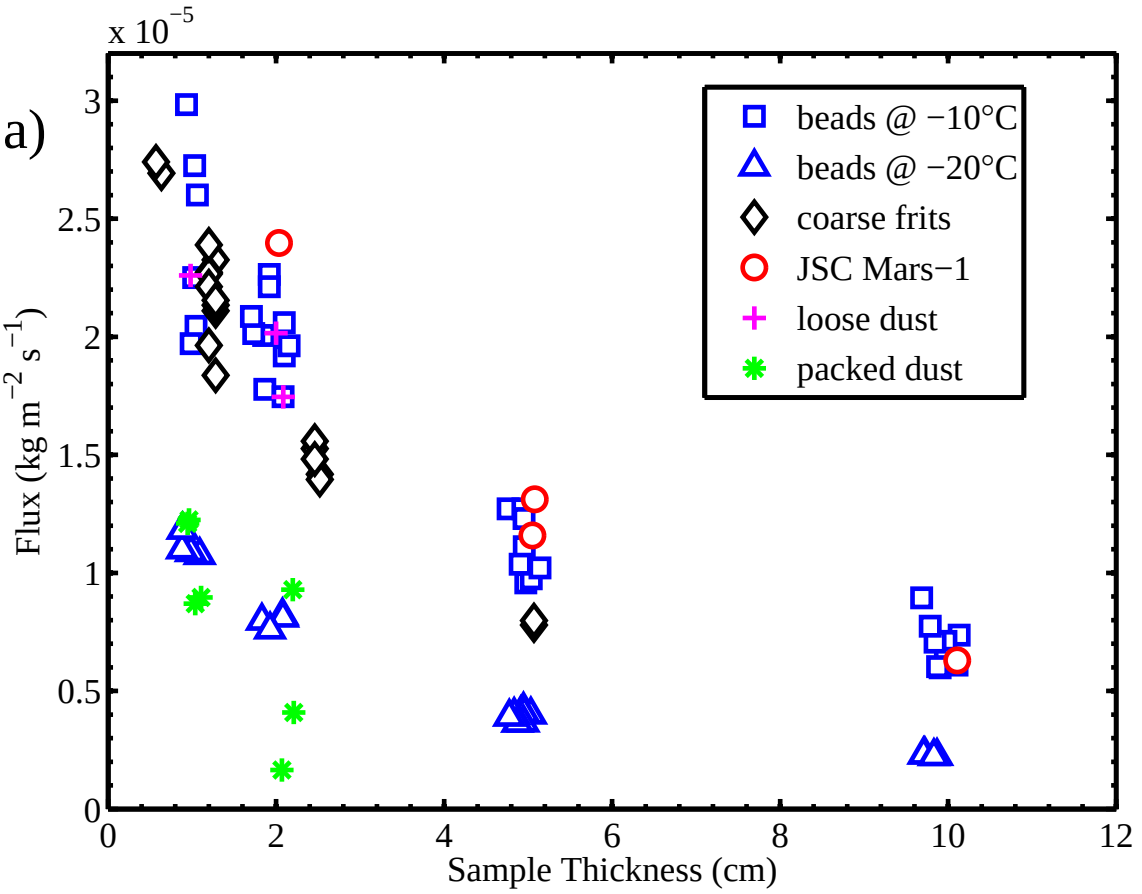

Figure 3.9: Flux versus sample thicknesses for each simulant as measured at 600 Pa and 263 K unless otherwise noted. Errors in flux are smaller than the symbols. The fluxes fall along the same curve for most experiments, notable exceptions being packed dust (asterisks) and 253 K experiments on glass beads (triangles).

that particle size and packing density, through their effect on the obstruction parameters ϕ and τ, are more important than particle shape (compare glass beads to frits), composition (compare glass simulants to JSC Mars–1), and size distribution (compare loose micron dust to other simulants).

When extrapolated to the Mars-appropriate temperature of 200 K, the diffusion coefficients obtained for samples other than packed dust fall in the range of 1.9–4.8 cm^2 s^{-1}. Both this and the 260 K values are at the low end of the range of 0.4–13.6 cm^2 s^{-1} given by *Flasar and Goody* (1976).

The tortuosity of the non-dust samples exhibits a range from 1.5 to 3.9. The tortuosity determined for high-pressure samples is closest to the true value, determinations made with equation (2.3) being overestimates when the diffusion regime is in transition. For the loose dust, calculations of τ with either equation (2.13) or equation (2.3) give similar results. Dust, whether loose or packed, exhibits a higher porosity. Given the results of *Clifford and Hillel* (1986), who show that larger pore spaces accommodate a majority of the flux, loose dust with large interstices between aggregates behaves as if it were in the Fickian regime with $r/\lambda_1 \approx 100/12 = 8.3$. A significant difference ($\sim 200\%$)

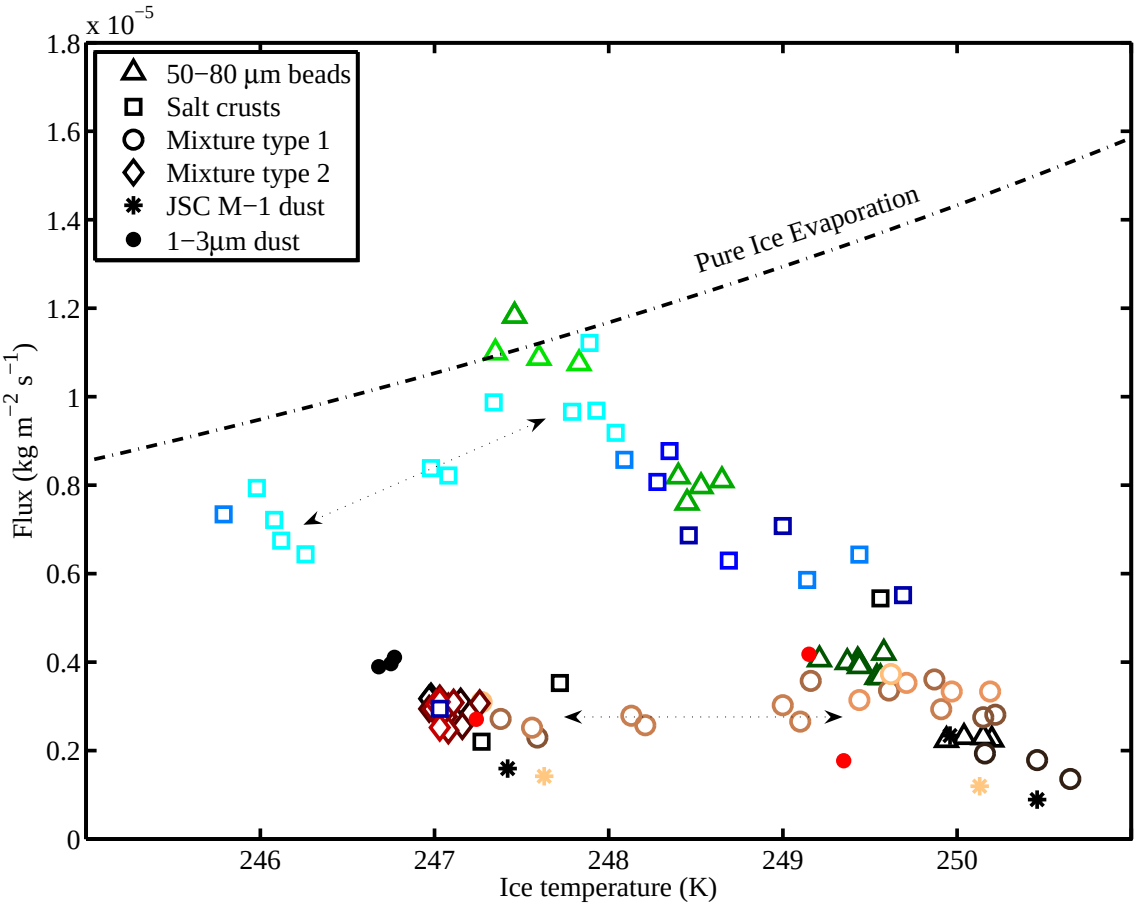

Figure 3.10: Flux versus ice temperature for each experiment; errors are smaller than the symbols. The dot-dashed line is the theoretical curve for evaporation of free ice into a dry atmosphere (*Ingersoll*, 1970). For a given sample, color trends from dark to light denotes decreasing resistance to diffusion (*e.g.*, lower thickness, dust content, or salt content). Arrows indicate trends within a single sample type as a function of temperature. See Section 4.2.1 for mixture type definitions.

results between the two calculation methods for τ when applied to the packed dust sample. Packed dust has only small pore spaces and its behavior is much closer to the Knudsen regime. Equation (2.13) may provide a more appropriate description in this case, though it still gives unusually high values of tortuosity: $\tau = 12.1 \pm 5.0$.

3.6 Discussion

The experimental setup simulates a static environment in which temperatures and humidities do not change significantly with time. A planetary subsurface is subjected to temperature and humidity variations on a variety of timescales, from diurnal to obliquity scale, which can affect the transport of water.

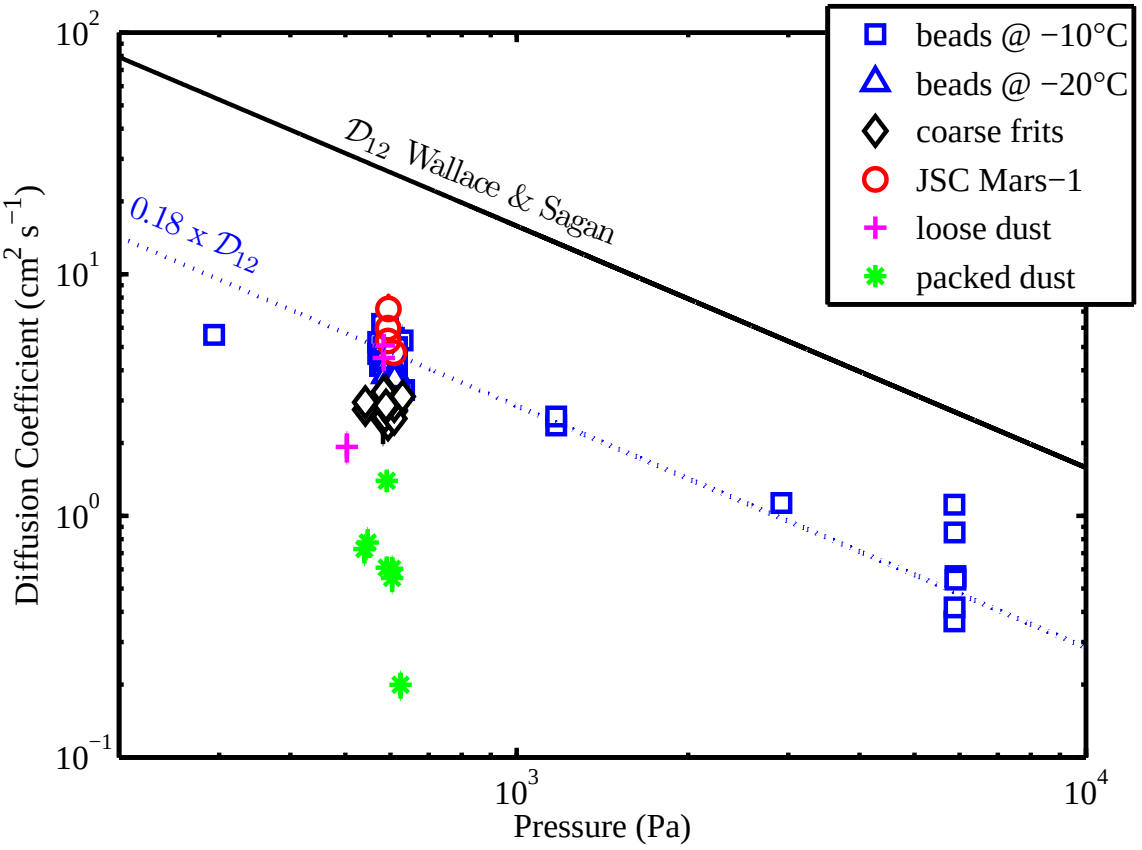

Figure 3.11: Diffusion coefficients versus pressure for all experiments. Errors in the diffusion coefficient are smaller than the symbols. The majority of experiments were run at 600 Pa. The solid line is the theoretically calculated value for the free-gas diffusion coefficient $\mathcal{D}_{12}$ as given by *Wallace and Sagan* (1979) for $T = 263$ K. The dotted line shows $\mathcal{D}_{12}$ scaled by an obstruction factor of 0.18. Packed dust falls below the trend of other experiments but 253 K experiments do not.

3.6.1 Adsorption

Rapid fluctuations in temperature arising from diurnal insolation changes could affect diffusion rates inasmuch as adsorption acts as a source or sink of water vapor. The non-equilibrium adsorption or desorption of water can have a significant effect on the instantaneous vapor density, and therefore on gradients in vapor density. Adsorption typically increases with partial pressure and therefore inhibits diffusion compared with a non-adsorbing environment by attenuating local vapor density gradients.

Adsorption results in a modification of the effective diffusion coefficient by a factor of $(1 + (1/\phi)\partial\alpha/\partial\rho_1)$, where ϕ is the porosity, α is the density of the adsorbed phase, and ρ_1 is the vapor density ((*Schorghofer and Aharonson*, 2005) and references therein). When $\partial\alpha/\partial\rho_1 = 0$, there is no adsorption. When $\partial\alpha/\partial\rho_1 = \infty$, there is complete adsorption of any additional water and $D = 0$. The term $\partial\alpha/\partial\rho_1$ for Mars temperatures is several orders of magnitude greater than unity according to *Zent and Quinn* (1995) and *Jakosky et al.* (1997).

This modification to the diffusion coefficient only applies when the system is out of equilibrium, when the adsorptive layer is undersaturated with respect to the local temperature and pressure and water adsorbs to the grain surfaces. If the temperature and local vapor density remain constant, the quantity of adsorbed water does not change with time; *i.e.,* no net exchange between the vapor and the adsorbate. Hence, in an environment that is temporally isothermal and isobaric, the diffusion remains unaffected by the adsorption after each local point in the regolith has reached an equilibrium with the vapor. Thus, the static experimental setup only experiences adsorptive effects in the initial moments of exposure of the ice to the soil, and they disappear by the time the thermal transients have passed (see Section 3.5.1.4 for a discussion of experimental absorptive saturation timescales).

The maximum temperature fluctuation experienced by the sample after initial transients occurs at its upper surface and will be no greater than the maximum air temperature fluctuations (± 0.45 K). With a specific surface area for glass beads between 0.015 and 0.03 $m^2\ g^{-1}$, such a change corresponds to a change in adsorbed mass of less than 1 $\mu g\ cm^{-3}$ (using the empirical isotherm presented by *Zent and Quinn* (1997) for the data of *Fanale and Cannon* (1971, 1974)). With these conditions the influence of adsorption cycles in these experiment is negligible.

On Mars, the scenario where adsorption has the greatest affect on the diffusion of vapor will be if adsorption proceeds from saturation to complete dessication and back over each cycle. The skin depth of adsorption and desorption is less than the thermal skin depth (*Jakosky*, 1983)

Adsorption on Mars greatly affects vapor density gradients on diurnal timescales, but long-term subsurface ice evolution depends on average gradients and adsorption has no accumulated effect (*Jakosky*, 1985; *Mellon and Jakosky*, 1993; *Schorghofer and Aharonson*, 2005). Thus these static experimental results are applicable to long-term near-surface ice evolution on Mars.

3.6.2 Temperature oscillations

The surface of Mars experiences large diurnal and seasonal temperature variations. The mean diffusive flux from a buried ice layer can be calculated using mean annual vapor densities (*Schorghofer and Aharonson*, 2005). The time-averaged density gradient in equation (2.2) is the same as the gradient of the time-averaged density, because the time integral and the spatial gradient can be interchanged. Neglecting the temperature dependence of the diffusion coefficient, one can then express the diffusive flux as $\langle J_1 \rangle = -D\langle \partial \rho_1 / \partial z \rangle = -D \partial \langle \rho_1 \rangle \partial z$. Angle brackets indicate a time average.

In the intervening layer between the ground ice and the atmosphere, frost and adsorbed water may form periodically. Unless stable throughout the year, this water will be lost again at a different time during the annual cycle and has no accumulated effect. In the long-term, it contributes nothing to the net vapor flux.

The mean vapor density gradient is simply $\partial \langle \rho_1 \rangle / \partial z \approx \Delta \langle \rho_1 \rangle / \Delta z$, where $\Delta \rho_1$ is the difference

between the vapor density at the surface and at the subsurface ice, and Δz is the spatial separation between these two points. For all but the most rapid timescales, mean annual values of vapor density control the evolution of subsurface ice. Since mean annual values govern the net transport, diffusion coefficients obtained from static experiments are applicable to the time-varying conditions on Mars.

3.6.3 Ice table evolution

Investigation by *Smoluchowski* (1968) of conditions which would permit long (>10 Gyr) survival times for buried ice was motivated by the assumption that Mars' climate may have allowed ice to be deposited at low latitudes very early in its history, but has remained essentially unchanged from its current conditions for the past ∼3.5 Gyr. To obtain such survival times in a completely dry atmosphere, his calculations assume extremely low porosities which lead to very low diffusion coefficients.

The water content of Mars' atmosphere is not zero; the current mean annual vapor pressure of water at the surface is ∼0.13 Pascals (*Farmer and Doms*, 1979; *Smith*, 2002). This small but non-zero quantity of atmospheric humidity introduces a frostpoint temperature of 198 K and thereby establishes an ice table equilibrium depth. The ice table will move until the mean annual vapor density above the ice is equal to the mean annual vapor density in the atmosphere and will thereafter be stationary until either its temperature changes or the atmosphere becomes more or less humid.

The equilibrium position of the ice table is not determined by regolith diffusivity, but solely by subsurface temperature and atmospheric water content. If ice is found (*e.g.,* through neutron spectroscopy, ground-penetrating radar, or trenching) to exist at a position away from the expected depth of equilibrium with respect to the current climate, it is possible that some transport-limiting process is slowing down the adjustment of the ice table.

Smoluchowski's work was based on the additional assumption that Mars' climate has been static for most of its history. More recent investigations (*Toon et al.* (1980) and many others since) have revealed that significant climatic variation occurs on more frequent timescales. Obliquity cycles of 125 kyr and 1.3 Myr and a longitude-of-perihelion precession with a 75 kyr period have dramatic effects on ice stability through the climatic variables of subsurface temperature and atmospheric water content (*Fanale et al.*, 1986; *Mellon and Jakosky*, 1995; *Zent and Quinn*, 1995). Assuming climate conditions on Mars were similar to their current state beyond several hundred thousand years in the past is therefore unrealistic.

The vapor transfer between the atmosphere and an ice-rich layer buried by a thickness, L, of porous medium is $J = D\Delta\langle\rho_1\rangle/L$. The rate at which the ice table evolves toward its equilibrium depth in response to a change in climate depends, therefore, on the value of D, and also on the vapor density difference between the saturated vapor above the ice and the atmosphere $\Delta\rho_1$, and the thickness of ice added or removed Z (positive downward). These terms are related by the

expression:

$$-\frac{d\mathrm{Z}}{dt} = -\frac{D\Delta\rho_1}{\rho_{\mathrm{ice}}}\frac{1}{\mathrm{Z}(t)} \tag{3.8}$$

where ρ_{ice} is the density of bulk ice. For a dry regolith of thickness L overlying pure ice, the loss of an ice layer of thickness, Z, in time, t, is given by

$$\mathrm{Z}(t) = \frac{D\Delta\rho_1}{\rho_{\mathrm{ice}}L}t. \tag{3.9}$$

Assuming that subsurface ice can be recharged during more favorable times, a conservative estimate for the maximum lifetime of a buried ice layer during a period of desiccating climate may be calculated by equation (3.9).

As an example, a 3% change in diffusivity at constant temperature would change the ice lost in one year by 3%. While diffusivity is a first-order control on the rate of subsurface ice evolution, its importance is dwarfed by the effects of subsurface ice temperature, particularly near the frostpoint. If the ice is near the frostpoint, a change by 5 degrees (less than 3%), from 200 to 205 K for example, will cause a 700% change in $\Delta\rho_1$. At higher temperature, a change of slightly less than 2%, from 260 to 265 K, will only change $\Delta\rho_1$ by 64%, but the absolute magnitude of the change will be much greater. In terms of ice loss, the former case means the difference between 3.6 and 24 millimeters of ice per year (a factor of $\sim$7), while the latter is the difference between 34 and 22 meters of ice per year ($\sim$50%).

Consider the evolution of a layer of near-surface ice for $\sim$38 kyr. This is one half-period of the shortest orbital climate variation (longitude-of-perihelion precession) and could represent the longest time during which the climate is in a single mode (*e.g.,* ice-loss) for some location on Mars. The depth of burial which would allow one meter of pure ice to retreat in this time by the method of equation (3.9) is presented in Figure 3.12 as a function of ice temperature.

If the ice fills interconnected pore spaces of a structural regolith matrix with low porosity ϕ, the removal of ice leaves behind a lag which increases in thickness. For a growing lag, L becomes $\mathrm{Z}(t)$ in (3.8) which makes t quadratic in Z. After integration,

$$\mathrm{Z}(t) = \left[\frac{2D\Delta\rho_1}{\rho_{\mathrm{ice}}}t + \mathrm{Z}^2(0)\right]^{\frac{1}{2}}. \tag{3.10}$$

The effect of the value of the diffusion coefficient on ice retreat depth versus time is shown in Figure 3.13 for ice at 200 K in a dry atmosphere for both "constant thickness" and "lag-forming" cases.

Relatively large diffusion coefficients of around 3 $\mathrm{cm}^2\ \mathrm{s}^{-1}$ allow ice to respond quickly to a climate change. Within one half-period of the 75 kyr climate cycle, a pure ice table buried by one meter of dry regolith could retreat to a depth of 19 cm. A pore-filling ice table initially retreats at about the

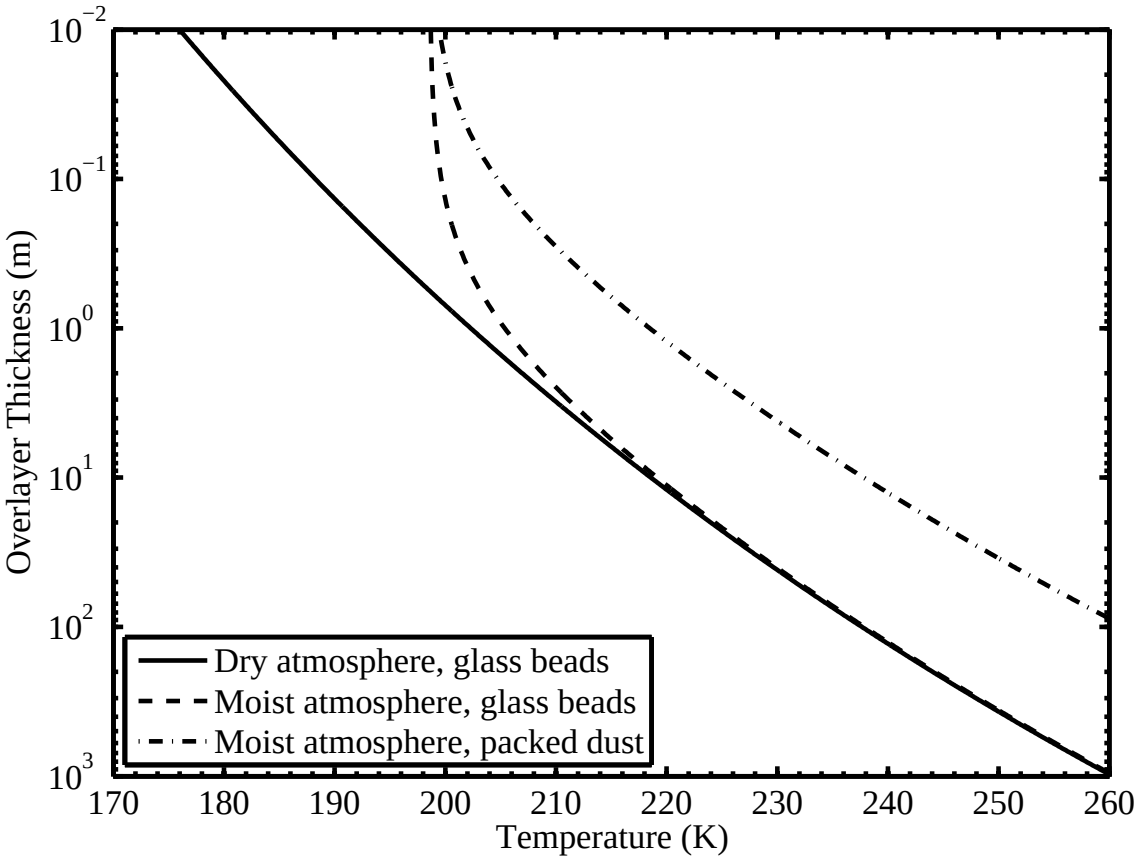

Figure 3.12: Regolith overlayer thickness required to allow one meter of ice retreat in ∼38 kyr (one-half of the 75 kyr climate cycle). The diffusion coefficients used are those extrapolated to 200 K via $D \propto T^{3/2}$ for glass beads and $D \propto T^{1/2}$ for packed dust, as appropriate for Fickian and Knudsen extrapolations, respectively. The values are in Table 3.2. The solid line represents zero atmospheric vapor density. The broken lines assume a present-day atmospheric vapor pressure of 0.13 Pa. With non-zero atmospheric humidity, ice is stable below the frostpoint and the overlayer thickness asymptotically approaches zero at this temperature (here, 198 K).

same rate because the area of ice exposed is reduced by the same factor ϕ as the volume density of ice, and would reach 60 cm in the same amount of time. A diffusion coefficient of 0.3 cm^2 s^{-1} causes the ice to respond more slowly and less than 1.9 cm of retreat is possible for a pure ice case in the same time. Warmer ice responds much more quickly: at 240 K, pure ice covered by one meter of regolith with $D = 0.3$ cm^2 s^{-1} would retreat by more than 700 cm in 38 kyr.

For the range of diffusivities measured in these experiments, the depth over which ice can respond to ∼100 kyr climate cycles is less than approximately one meter. This is similar to the difference in ice table equilibrium depths determined for a range of obliquities in the model of *Mellon and Jakosky* (1995). Whether or not present-day subsurface ice has responded to recent climate variations and is at its equilibrium depth with respect to the current climate will depend both on the ice temperature, the diffusivity of the overlying regolith, and whether the ice is a pore-filling substance or is a solid

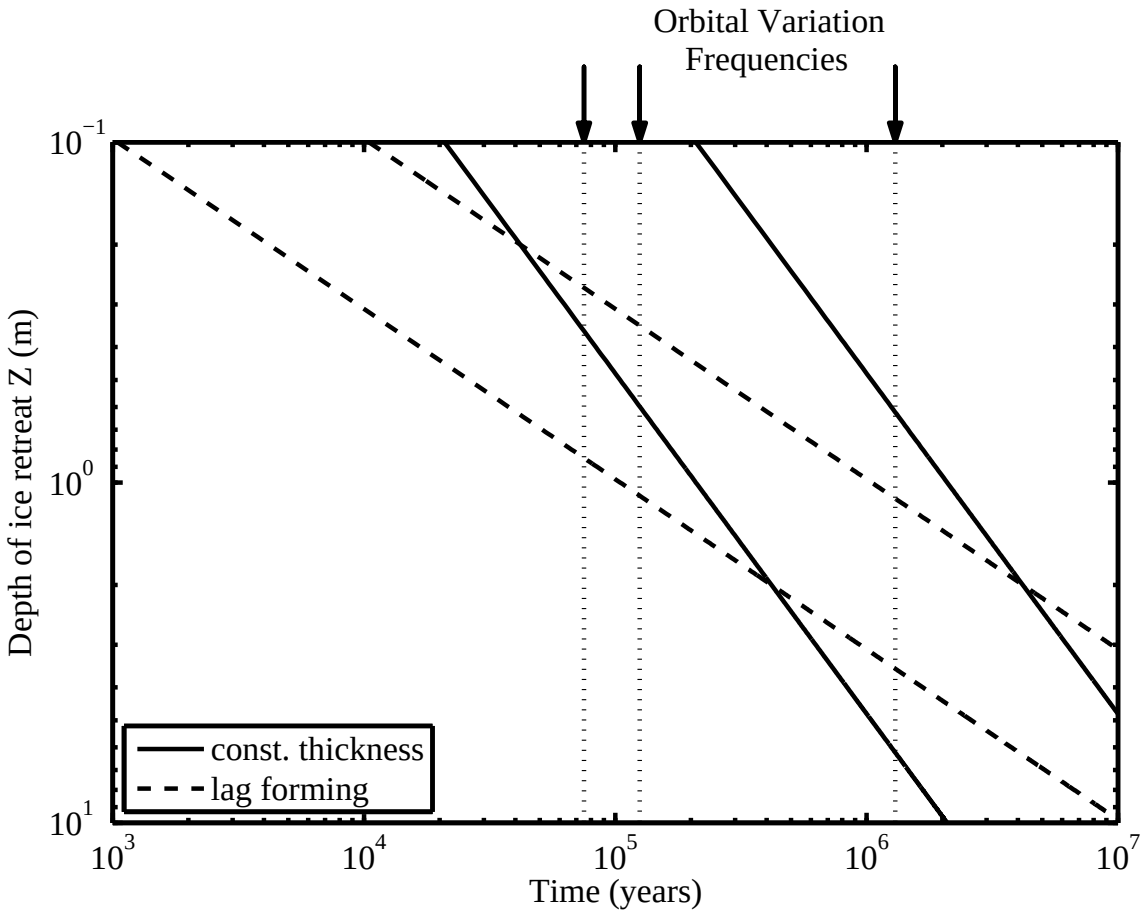

Figure 3.13: Retreat depth versus time for two values of the diffusion coefficient in a moist atmosphere. Solid lines show cases for pure ice under a regolith one meter thick. Dashed lines show lag-forming cases with an initial barrier of 1 mm. Values of D used are 3.0 cm^2 s^{-1} for the left lines, and 0.3 cm^2 s^{-1} for the right lines. $T_{\rm ice} = 200$ K. Vertical dotted lines are, from left to right, the frequencies of 75, 125, and 1300 kyr climate cycles.

slab of pure ice.

For cases with very high ice filled porosity, *e.g.,* polar layered deposits where the material is likely to be only a few percent dust, a lower porosity lag will still form as the ice sublimates.

This simple model is limited by the assumption of isothermal ice in equations (3.9) and (3.10) and Figure 3.13. As the ice front moves, its mean annual temperature will adjust to that specified by the soil thermal properties and the insolation at the surface. Soil thermal properties are very likely to be correlated with mass-transport diffusivity. Low density materials with a small amount of interconnectivity between individual grains (such as dust) are likely to have low thermal conductivities and hence low thermal inertias.

3.6.4 Diffusion in Mars surface processes

The degree to which the ice beneath a given regolith will be able to respond to variations of a particular frequency will depend on the value of the diffusion coefficient, lower values of D corresponding to a more sluggish response. Evidence for near-surface ice from Mars Odyssey (*Boynton et al.*, 2002; *Feldman et al.*, 2004b) is consistent with climate model predictions which imply that the present-day Mars ice tables are at or near their equilibrium positions with respect to the present climate (*Mellon and Jakosky*, 1993; *Mellon et al.*, 2004; *Schorghofer and Aharonson*, 2005). This suggests rapid communication between the subsurface ice and the atmosphere. *Schorghofer and Aharonson* (2005) estimate that a diffusivity of at least 1 $\mathrm{cm}^2\ \mathrm{s}^{-1}$ is required to achieve the observed balance between atmospheric water vapor and ground ice distribution within a single obliquity cycle. On timescales of years or decades, the coupling of atmospheric water circulation with the regolith will be strongest in soils with rapid diffusion. An upper limit on realistic soil diffusivities will set the maximum adjustment rate of subsurface ice to climate fluctuations.

Likewise, the lowest realistic soil diffusivity sets the minimum adjustment rate of subsurface ice to climate fluctuations. With $D = 1\ \mathrm{cm}^2\ \mathrm{s}^{-1}$ at 200 K and in a dry atmosphere, ice in the top meter can be sustained for at most 80 kyr. This result is obtained by inverting equation (3.10) for the time t it takes to retreat to depth Z, $t = (\mathrm{Z} - \mathrm{Z}_0)^2 \rho_{\mathrm{ice}} / (2D\Delta\rho_1) \leq \mathrm{Z}^2 \rho_{\mathrm{ice}} / (2D\Delta\rho_1)$.

The subsurface temperature cannot be expected to stay constant for longer than a few tens of thousands of years because of orbital variations in insolation. Variations on these longer timescales will be able to affect ice beneath porous regoliths with lower values of D. Additionally, during times of high atmospheric humidity the mean gradient in vapor density at particular latitudes may either vanish, resulting in stable subsurface ice, or reverse, resulting in ice accumulation.

Significant variability in the diffusive properties of the Martian regolith at different locations and depths is expected. The range of pore sizes and values of D given by the investigators mentioned in Section 1.2.2 reflects this uncertainty. In the absence of any global-scale data on regolith porosities or other quantities that would enable the calculation of D, most existing models incorporate spatially homogeneous diffusion coefficients.

These results are important in light of the frequent use of diffusivity of regoliths as inputs to models. Long-term models of the Mars water cycle will be affected by the distribution and extent of lower-diffusivity regoliths which act as sluggish sinks or sources of atmospheric water. In their work considering the recent history of the northern polar layered deposits, *Levrard et al.* (2005) present as a possibility the "common presumption" than dust-containing polar water ice could form a thick lag deposit upon sublimation which would protect deeper ice. They introduce a factor f which reduces the flux when covered by a growing lag. This factor is directly related to the obstruction factor ϕ/τ; values of ϕ/τ determined through these experiments can inform estimations of the factor f.

Skorov et al. (2001) claim that pore radii in Mars regoliths are between 0.1 and 10 microns

and therefore Knudsen conditions obtain. In the same sentence, however, they say that sand- and granule- sized "clodlets" are present. The experiments in this chapter with uncompacted dusts suggest that the presence of such clodlets (in particular, the void spaces between them) would enhance the proportion of Fickian diffusion.

In papers considering conditions which could give rise to transient liquid water on present-day Mars, *Hecht* (2002), *Clow* (1987), and *Farmer* (1976) point out that the presence of a snow or dust cover can significantly suppress evaporative cooling. This circumvents the limitation identified by *Ingersoll* (1970) that evaporative cooling exceeds the solar constant already at temperatures below melting. The reduced heat loss allows ice in favorable environments to reach the melting point. The possibility of transient liquid applies both to the formation of geomorphic features such as crater-wall gullies and sub-glacial drainage networks, and also to problems of water availability for possible Martian organisms.

Other investigators invoke low values of diffusivity as well. *Murray et al.* (2005) suggest that a near-surface barrier with a low diffusion coefficient could explain geomorphic features in Cerberus Fossae as persistent equatorial ice rafts that have remained since the last eruption of water from Cerberus. *Head et al.* (2005) invoke low diffusion coefficients to explain the possible existence of tropical glaciers on Mars. Appropriately for greater depths where porosity may be greatly reduced, *Krasnopolsky et al.* (2004) and *Weiss et al.* (2000) assume a small pore size of order microns when considering the diffusion of methane and other gases.

The experimental findings presented here show relatively high values of D for a range of unconsolidated regolith types. Lower values, such as would be required by the arguments of some of the investigations above, only appear in mechanically modified soils.

3.6.5 Mars regolith properties

The combined results of the experimental investigations and the calculations presented in this section are applicable to Mars only insofar as reasonable estimates of true regolith properties can be made. Dunes and other aeolian landforms indicate the widespread presence of particulate matter with sand-sized grains. Atmospheric scattering effects and observations by surface landers verify the global presence of very fine dust.

The Mars Exploration Rovers (MER) both see soils composed of rounded grains with a maximum size of 100 μm. Grain sizes extend down to the limit of resolution of the Microscopic Imager, but the size distribution down to micron-size dust is not known. The soil compositions are remarkably uniform across the five landing sites of Viking, Pathfinder, and MER, having more in common with each other than the analyzed rocks at those sites (*Yen et al.*, 2005). Since aeolian processes are efficient at sorting grain sizes, it is possible that areas exist on Mars where the regolith is composed of windblown sand particles of nearly homogeneous size. Other areas may be dust laden and better

represented by micron or sub-micron sized dust.

Putzig et al. (2005) have used Thermal Emission Spectrometer (TES) observations of Martian surface thermal properties to estimate global thermal inertia at 3 km resolution. Along with earlier work by *Kieffer et al.* (1973) and *Christensen* (1986), these observations show that Mars' surface has large regions with a significant fraction of unconsolidated dust ($\leq$ 40 μm). Such materials are characterized by low thermal inertias, while both sand-sized particles and indurated fines can give intermediate values between loose dust and solid rocks. At 600 Pa, dust particles with diameters $\leq$ 2 μm will exhibit primarily Knudsen diffusion if the pore sizes are comparable to the grain size. The results presented here suggest that this condition only obtains when the dust has been packed by some mechanism. Regardless of how the dust is compacted, its thermal inertia will be higher than loose air-fall dust. Moderate thermal inertia regions indicative of a high proportion of sand-sized particles (approximated by the 50–80 μm beads) would fall in the transition region between Fickian and Knudsen diffusion.

In their theoretical investigation of the effects of pore size distribution on subsurface ice survival, *Clifford and Hillel* (1983) calculated flux distributions through 12 model pore size distributions. Their results showed that in all cases of non-uniform pore size, the largest pores always accounted for the highest percentage of total flux. They thus concluded that the geometric factor which most significantly influences ground ice loss rates (other parameters like temperature and humidity being equal) is the porosity characterized by the larger ($\geq$ 1 μm in their simulants) pores. Real soils almost always have polydisperse grain sizes, and it is likely that aggregation operates on Mars as least as efficiently as it does on the Moon. If a soil has more than a few percent of its pore space accommodated by statistically larger pores, the diffusion will be dominated by these more open pathways. Despite the presence of small pore spaces, the whole soil could have a diffusivity comparable to a monodisperse soil with an average pores size equal to its largest pores to within about 10–15% (*Clifford and Hillel*, 1983).

3.6.6 Obtaining low diffusivity on Mars

The experiments described in this chapter indicate that, for a variety of simulants with a range of particle sizes, shapes, and pore-space geometries, diffusivities under Martian surface conditions will be on the order of 2.8–5.4 cm^2 s^{-1}, the obstruction factor being between 0.09–0.21. Mechanically packing well-sorted large grains does not significantly reduce the diffusivity, and neither gravitational nor near-surface compressive packing will result in a substantial change in pore geometry. Evidence of dust deposition at lander sites and low thermal inertia values observed from orbit suggest a range of physical properties consistent with most shallow Martian sediments being porous and allowing significant diffusion of vapor (*Jakosky*, 1983). The values of D given above are significantly higher than those invoked by some papers referenced in Section 3.6.4.

The shape of dust can affect its diffusive properties. Micron-size particles are not easily abraded and often exhibit angular forms whose irregular edges easily interlock and prevent more efficient packing arrangements. Even perfectly spherical particles may agglomerate because of electrostatic forces or by cohesion due to adsorption of water. Whether deposited as individual grains or as millimeter to sub-millimeter scale aggregates, the structure of air-fall dust deposits is likely to be much more open than the physical packing limit, and the obstruction factor may be near the value of 0.18 observed for loose dust samples.

The simple idea of having wind-blown dust of the smallest particle sizes settle into the pore spaces of coarser exposed surface material, thereby blocking the escape of water vapor molecules, may not in fact produce the expected small effective diffusion coefficient. The results obtained here suggest that, in the absence of mechanical packing, the diffusion coefficient of the micron-sized particles is not very different from that of the larger particles.

A few purely mechanical process could operate on Mars and provide the packing force required to produce a significant reduction in the observed D (as was necessary for the laboratory measurements). Processes which result in systematically closer packing of the very fine particles, such as sedimentation or cementation, to produce a less porous layer (or the in-filling of the larger voids) could plausibly produce more resistive vapor transport barriers than simple wind-blown redistribution of the dust.

Examples of processes which will produce low diffusivity barriers with micron-size dust are:

Caliche or duricrust: Indurated soils, often described as "duricrust", have been observed at Viking, Pathfinder, and MER landing sites. No conclusive observations of the chemistry of these crusts yet exist, but it is likely that cementation by mobile salts plays a role in their formation. Additionally, subsurface salts deposits have been observed at the MER landing sites (*Cabrol et al.*, 2006; *Yen et al.*, 2007; *Wang et al.*, 2007) and salt is known to be an important component of the martian regolith (*Clark and van Hart*, 1981; *Vaniman et al.*, 2004; *Yen et al.*, 2005). Under certain conditions these could form subsurface cemented layers, similar to terrestrial caliche, which could impede the flow of water vapor.

Settling in liquid water: Water can deflocculate dust aggregates, mitigate electrostatic repulsion, and lubricate the sliding of angular particles, all of which permit higher packing densities. In their paper where they consider Knudsen diffusion on Mars through mixtures of small ($\leq$10 μm) particles, *Clifford and Hillel* (1983) model their distributions after natural samples which have been sedimented in fluid and then dried. The MER rover Opportunity has discovered evidence for shallow standing water on Mars' surface at some point in the past (*Squyres et al.*, 2004a). Whether any dense layers of small particles formed at such times could have survived unbroken to the present is unknown, but seems unlikely. Additionally, dense layers formed in standing

water have a tendency to crack upon subaerial drying, as observed on playas in terrestrial deserts and mud flats.

Physical packing: This process, requiring a significant downward force, is unlikely to act over broad areas unless large-scale burial of a region compacts previously emplaced dust. This mechanism may operate in the formation and subsequent burial by fresh ice of polar layers. Exhumation processes may destroy whatever cohesive layers were formed, although still-buried dense layers of dust are possible. Additionally, mixtures of polydisperse grains which have less than a critical dust content (i.e. the quantity of fine dust required to fill the larger pore spaces) will not pack more tightly than is allowed by the larger grains under the moderate pressures experienced in the upper few meters of a regolith column.

There are few investigations into the porous geometry of martian air-fall dust in the literature. *Moore* (1987) discusses the density and probable particle size composing "drift material" at Viking lander sites. A number of criteria suggest that the drift material examined by Moore is from 0.1–10 μm in size. The observed density of 1.0–1.3 g cm^{-3} would, for basaltic material, correspond to a porosity of 44–66%. Such low porosities cannot be attained with the micron-sized dust used in these experiments without dispersal in water. The drift material may have been subject to some porosity-reducing surface process.

Further studies are needed on the processes of dust deposition under Mars surface conditions so that pore size distributions for dust can be estimated for a wide range of particle sizes and shapes. Based on the current understanding of Mars soils and these laboratory observations, it seems difficult to produce low diffusivity barriers, except perhaps by the action of liquid water, chemical deposition, or both.

Investigations on Mars processes that invoke low diffusivity materials should address the formation mechanism of such barriers. Porous media with moderate diffusivities ($\sim$2–5 cm^2 s^{-1}) are easily formed from a variety of regolith materials, but lower diffusivities are difficult to obtain even in the presence of micron-sized dust.

3.6.7 Conclusions

These experiments have measured diffusion coefficients in several regolith simulants under conditions of sublimation and at pressures appropriate to the surface of Mars. The experimental setup used mimics the geometry and environment of martian subsurface ice overlain by a porous material. Diffusion coefficients are obtained from mass loss, ice temperature, humidity, and sample thickness; simulant porosity and chamber pressure are also measured. The vapor transport theory of Chapter 2 is applicable not only to the experimental setup, but also to variable pressure and temperature environments as exist on Mars.

Previous considerations of diffusive processes on Mars have been primarily based on the kinetic theory of gases in porous media or on experiments at conditions significantly different from those on the martian surface. These studies suggest a wide range of possible values of the diffusion coefficient, from a high of 13.6 $cm^2\ s^{-1}$ to a low of 0.4 $cm^2\ s^{-1}$ for unconsolidated near-surface regoliths, with values on the order of 10^{-3} $cm^2\ s^{-1}$ for extremely low porosity materials.

Experiments with glass beads in the 50–80 μm size range are a proxy for aeolian sediments on Mars. Measured at a pressure of 600 Pa, the diffusivity is determined to be $D = 4.49 \pm 0.69$ $cm^2\ s^{-1}$. The obstruction factor is determined to be 0.17 ± 0.03 and measured porosity is $44 \pm 2\%$.

Data taken over a range of pressures and thicknesses provide a Fickian and a Knudsen diffusion coefficient for 50–80 μm glass beads. The pressure-dependent Fickian diffusivity is (600 Pa/p_0) $\times$ 6.5 $cm^2\ s^{-1}$ and the Knudsen diffusivity is 9.8 $cm^2\ s^{-1}$. The crossover pressure where dominance changes between one regime and the other is found to be about 398 Pa. This is consistent with the definition of the transition region as given by the ratio of mean pore size to mean free path (r/λ_1). The pressure-independent tortuosity in the Fick regime 1.7 ± 0.6, a value significantly smaller than the value of $\tau = 5$ given by Smoluchowski (and quoted by some subsequent investigators) for porosities around 50%.

The highest experimentally measured diffusivity is 7.2 $cm^2\ s^{-1}$ for a thin sample of JSC Mars–1, which exhibits an obstruction factor of 0.27 ± 0.03. A number of other simulants (porous fritted disks and loose 1–3 μm dust) have diffusivities similar to the glass beads. The range covered by these simulants is 2.8–5.4 $cm^2\ s^{-1}$ (see Table 3.2). The only observation of a significantly reduced diffusivity is with mechanically packed 1–3 μm dust which exhibits an average D of 0.38 ± 0.26 $cm^2\ s^{-1}$. Diffusion coefficients are slightly reduced when extrapolated to 200 K using either the Fickian ($T^{3/2}$) and Knudsen ($T^{1/2}$) temperature dependencies (also in Table 3.2).

The variation of D among experiments with the same simulant is 8 to 16% for non-dust samples. Gravity, adsorption, and other forms of diffusion have been shown to play no significant role in the experiments.

While the vapor density over ice as a function of temperature is a very strong determiner of the equilibrium position and evolution rate of subsurface ice, the diffusivity of the overlying regolith is also a first-order control on the rate of subsurface ice migration. In extreme cases, low diffusivity barriers could act to protect buried ice from being lost during periods of dry climate as suggested by *Smoluchowski* (1968).

There are few purely mechanical process on Mars which could produce a significant reduction in porosity for micron-sized air-fall dust, thereby obtaining a diffusivity similar to Smoluchowski's low values. Invoking significant reduction of D requires an explanation of which processes lead to the formation of the low diffusivity barrier and how those processes fit in context with other observations. There are a number of processes which may give rise to such barriers. The efficacy of such processes

and their prevalence on past and present-day Mars warrant further study. In Chapter 4, the efficacy of particle-size mixtures, salt-cemented sediments, and dusts to act as barriers to vapor diffusion are explored.